



Temperature and strain controls on ice deformation mechanisms: insights from the microstructures of samples deformed to progressively higher strains at -10, -20 and -30°C

Sheng Fan¹, Travis Hager², David J. Prior¹, Andrew J. Cross^{2,3}, David L. Goldsby², Chao Qi⁴, Marianne Negrini¹, John Wheeler⁵

¹ Department of Geology, University of Otago, Dunedin, New Zealand

² Department of Earth and Environmental Science, University of Pennsylvania, Philadelphia, PA, USA

³ Department of Geology and Geophysics, Woods Hole Oceanographic Institution, Woods Hole, MA, USA

⁴ Institute of Geology and Geophysics, Chinese Academy of Sciences, Beijing, China

⁵ Department of Earth and Ocean Sciences, University of Liverpool, Liverpool, UK

Correspondence to: Sheng Fan (sheng.fan@postgrad.otago.ac.nz).

Abstract Understanding ice deformation mechanisms is crucial for understanding the dynamic evolution of terrestrial and planetary ice flow. To understand better the deformation mechanisms, we document the microstructural evolution of ice with increasing strain. We include data from deformation at relatively low temperature (-20 and -30 °C) where the microstructural evolution has never before been documented. Polycrystalline pure water ice was deformed under a constant displacement rate (equal to the strain rate of $\sim 1.0 \times 10^{-5} \text{ s}^{-1}$) at temperatures of -10, -20 and -30 °C to progressively higher true axial strains (~3, 5, 8, 12 and 20%). Mechanical data show peak and steady-state stresses are larger at colder temperatures as expected from the temperature dependency of creep. Cryo-electron backscattered diffraction (EBSD) analyses show distinct sub-grain boundaries in all deformed samples, suggesting activation of recovery and subgrain rotation. Deformed ice samples are characterised by “big grains” interlocking with “small grains”. For each temperature series, we separated “big grains” from “small grains” using a threshold grain size, which equals to the square mean root diameter at ~12% strain. “Big grains” are more lobate at -10 °C than at colder temperatures, suggesting grain boundary migration (GBM) is more prominent at warmer temperatures. The “small grains” are smaller than subgrains at -10 °C and they become similar in size at -20 and -30 °C, suggesting bulge nucleation facilitates the recrystallization process at warmer temperature and subgrain rotation recrystallization is the nucleation mechanism at colder temperatures. At temperatures warmer than -15 °C, *c*-axes develop a crystallographic preferred orientation (CPO) characterized by a cone (i.e., small circle) around the compression axis. We suggest the *c*-axis cone forms as a result of selective growth of grains at easy slip orientations (i.e., $\sim 45^\circ$ to shortening direction) by strain-energy driven GBM. This particular finding is consistent with previous works. The opening-angle of the *c*-axis cone decreases with strain, suggesting strain-induced GBM is balanced by grain rotation. Furthermore, the opening-angle of the *c*-axis cone decreases with temperature. At -30 °C, the *c*-axis CPO transits from a narrow cone to a cluster, parallel to compression, with increasing strain. This closure of the *c*-axis cone is interpreted as the result of a more active grain rotation together with a less effective GBM. As the temperature decreases, the overall CPO intensity decreases, facilitated by the CPO



weakening in “small grains”. We suggest the grain size sensitivity of grain boundary sliding (GBS) favours a faster strain rate in “small grains” and leads to the CPO weakening at cold temperatures. CPO development cannot provide a uniform explanation for the mechanical weakening (enhancement) after peak stress. Grain size reduction, which can be observed in all deformed samples, is most likely to cause weakening (enhancement) and should be considered to have a significant control on the rheology of natural ice flow.

1 Introduction

Glaciers and ice sheets play key roles in shaping planetary surfaces, and form important feedbacks with climate, both on Earth (Hudleston, 2015) and elsewhere in the solar system (Hartmann, 1980; Whalley and Azizi, 2003). Understanding the controls on the flow rate of terrestrial glaciers and ice sheets is crucial, as this will be a major control on future sea level change (Bindschadler et al., 2013; Dutton et al., 2015; Bamber et al., 2019). Terrestrial glacial ice flow is driven by gravity. Flow is facilitated both by sliding at the base of the ice and by the internal (creep) deformation of ice masses. The contribution of creep deformation to the total flow rate is controlled primarily by differential stress and temperature within the ice body (Rignot et al., 2011; Hudleston, 2015). Creep experiments show a change in the mechanical behaviour as initially isotropic polycrystalline ice is deformed (Faria et al., 2014; Hudleston, 2015). Mechanical weakening occurs during the transition from secondary creep (minimum strain rate) to tertiary creep (quasi-constant strain rate) in constant load experiments (e.g., Weertman, 1983; Budd & Jacka, 1989; Montagnat et al., 2015) and from peak stress to steady-state stress in constant displacement experiments (e.g., Durham et al., 1983, 2010; Vaughan et al., 2017; Qi et al., 2017). This mechanical weakening is often referred to as strain rate “enhancement” in the glaciological and ice sheet literature (Alley, 1992; Placidi et al., 2010; Treverrow et al 2012). Enhancement correlates with the development of a crystallographic preferred orientation (CPO) (Jacka and Maccagnan, 1984; Vaughan et al., 2017) and also with other microstructural changes, in particular grain size reduction (Craw et al., 2018; Qi et al., 2019). Understanding the deformation and recrystallization mechanisms responsible for ice microstructure and CPO development is therefore essential for quantifying how different mechanisms contribute to ice creep enhancement in nature. Moreover, the relative roles of intracrystalline plasticity, recrystallization and grain size sensitive mechanisms, especially at low temperatures, are not well known.

In this contribution we present microstructural analyses of samples deformed to successively higher strains through the transition from peak stress (secondary creep) to steady-state stress (tertiary creep) at -10, -20 and -30 °C. These conditions were chosen so that the experiments included evolution of CPO towards a cone (high temperature) and towards a cluster (low temperature). For the first time, we present ice microstructural data from samples deformed to progressively higher strains at -20 and -30 °C. Our objectives were to study the influences of temperature and strain on ice mechanical behaviour, microstructure and CPO development.



2 Methods

2.1 Sample fabrication

Dense, polycrystalline ice samples were prepared by the flood-freeze (standard ice) method (Cole, 1979; Durham et al., 1983; Stern et al., 1997) to meet the requirements of controlled grain size, random CPO and minimised porosity. We crushed ice cubes made from frozen Milli-Q water (ultra-pure water), into ice powders with a wide range of particle size. These ice powders were then sieved at $-30\text{ }^{\circ}\text{C}$ in a chest freezer, to limit the particle sizes to 180 to 250 μm . The particles were then packed into the bottom of greased stainless-steel cylindrical moulds (inner diameter 25.4 mm) to achieve a porosity of $\sim 40\%$. A perforated brass spacer was placed on top of the packed ice powder and the mould was sealed with a double O-ring plug. The assembled moulds were evacuated to near-vacuum state and equilibrated at $0\text{ }^{\circ}\text{C}$ in a water-ice bath for 40 minutes. Degassed Milli-Q water ($0\text{ }^{\circ}\text{C}$) was then flooded through the moulds filled with powder. After flooding, the moulds were transferred immediately to a $-30\text{ }^{\circ}\text{C}$ chest freezer. The moulds were placed vertically into cylindrical holes in a polystyrene block, with the base of moulds in contact with a copper plate at the bottom of the freezer. This ensures that freezing front migrates slowly upwards. The perforated spacer prevents ice particles from floating in the water. After 24 hours, the frozen moulds were extracted from the polystyrene block and the ice samples gently pushed out using an Arbor press. Both ends of the cylindrical samples were cut and polished to be flat, parallel with one another, and perpendicular to the sample's long axis. The length of each ice sample was recorded after the polishing (Table 1). Each of the samples was encapsulated in a thin-walled indium jacket ($\sim 0.38\text{ mm}$ wall thickness), the bottom of which had already been welded to a stainless-steel end-cap. After that, the top of each indium tube was welded to a steel semi-internal force gauge, with a zirconia spacer placed between the force gauge and sample. The sample was kept cold in a $-60\text{ }^{\circ}\text{C}$ ethanol bath (Qi et al., 2017) during welding.

2.2 Experimental set up and process

We conducted axial compression experiments on the ice samples at the Ice Physics Laboratory, University of Pennsylvania. Experiments were conducted at a nitrogen gas confining pressure of $\sim 20 \pm 0.5\text{ MPa}$ at temperatures of -10 , -20 , and $-30\text{ }^{\circ}\text{C}$ ($\pm 0.5\text{ }^{\circ}\text{C}$), in a cryogenic, gas-medium apparatus (Durham et al., 1983; Heard et al., 1990). Samples were left to thermally equilibrate with the apparatus for more than 60 minutes (at the experimental conditions) before deformation started. Deformation experiments were performed at a constant axial displacement rate, giving an initial constant strain rate of $\sim 1.0 \times 10^{-5}\text{ s}^{-1}$. The experiments were terminated once the final axial true strains of $\sim 3\%$, 5% , 8% , 12% and 20% were achieved. After that, the ice samples were immediately extracted from the apparatus, photographed and measured. Samples were cooled over ~ 15 minutes to liquid nitrogen temperature and stored in a liquid nitrogen dewar. Typical time between the end of the experiments and the start of cooling was between 10 and 30 minutes.



2.3 Mechanical data processing

During each experimental run, time, displacement and load were recorded at a frequency of 0.14–0.2 Hz. The axial stress was calculated from the load divided by cross-sectional area of the ice sample. The stress has been corrected for the change of sample cross-sectional area, assuming constant sample volume during the deformation. For each ice sample, we define the axial stretch λ (Eq. (1)) as the ratio of the sample length ($L(t)$) at time t and the initial sample length (L_0). The sample length $L(t)$ at time t is calculated from the displacement and the initial sample length (L_0). The true axial strain (ε) is defined in Eq. (2) (Hobbs et al., 1976).

$$\lambda = \frac{L(t)}{L_0} \quad (1)$$

$$\varepsilon = -\ln(\lambda) \quad (2)$$

10 2.4 Cryo-EBSD data

The recent development of cryo-EBSD technique provides an access to full crystallographic orientations and significant microstructural detail in analysing ice samples with large sizes (up to 70 mm by 30 mm) (Prior et al., 2015). We prepared the ice samples and acquired the cryo-EBSD data following the procedures described by Prior and others (2015). The samples were cut in half along the cylindrical long-axis by a band saw in a -20 °C cold room and a 5 mm slice was extracted from half of the sample. One side of the slice, at a temperature of ~-30 to -50 °C, was placed against a copper ingot (70 mm by 35 mm) at ~5 °C. The samples were placed in a polystyrene sample transfer box (~100 °C) as soon as a bond formed between the ice sample and the ingot (Prior et al., 2015). We acquired a polished sample surface for cryo-EBSD by hand lapping on grit paper. The samples were polished at ~-40 °C to 3.0-6.0 mm thick using grit sizes of 80, 240, 600, 1200 and 2400. Soon after, the sample-ingot assemblies were transferred to the polystyrene sample transfer box and cooled to close to liquid nitrogen temperature, before they were transferred to the SEM for the collection of cryo-EBSD data.

EBS data were acquired using a Zeiss Sigma VP FEGSEM combined with a NordlysF EBSD camera from Oxford Instruments. The sample-ingot assembly was transferred to a cold stage (maintained at ~-100 °C) fixed in the SEM chamber. We used pressure cycling in the SEM chamber to activate surface sublimation to remove frost and create a damage-free sample surface (Prior et al., 2015). EBSD data were acquired at a stage temperature of ~-95 °C, with 5-7 Pa nitrogen gas pressure, 30kV accelerating voltage and ~60 nA beam current. For each ice sample, we collected a reconnaissance map with a step size of 30 μm for the whole section. For detailed microanalysis, we also collected a map with the step size of 5 μm from a selected sub-area. We acquired and montaged the raw EBSD data by using the Aztec software. Details of the raw EBSD data have been summarized in Table 2.



2.5 Processing of the cryo-EBSD data

Ice microstructural parameters including grain size and grain boundary geometry are important indicators for inferring deformation processes. We quantified the microstructural parameters of ice grains from raw EBSD data using the MTEX toolbox (Bachmann et al., 2011; Mainprice et al., 2015) in MATLAB. The ice grains were reconstructed from the raw EBSD pixel map with 5 μm step size. We defined the ice grain boundaries where the misorientations between the neighbouring pixels were larger than 10° . We removed noise from the EBSD data by removing the grains containing fewer than 4 indexed pixels. No pixel interpolation was applied to the EBSD pixel map, preserving any non-indexed space. Grain size was determined as the equivalent diameter of a circle with the area equal to the measured area of each grain.

We quantified the geometrically necessary dislocations (GNDs) (Ashby, 1970) using the Weighted Burgers Vector (WBV) method (Wheeler et al., 2009). GNDs are the dislocations required to generate an observed lattice distortion (for example, a sub-grain boundary). The WBV method gives a weighted measure of the Burgers vectors of GNDs by defining the WBV as the sum, over all types of dislocations, of [(density of intersections of dislocation lines with a map) \times (Burgers vector)]. Note that the 3D density for each type of the dislocation is weighted by a parameter l , which depends on the angle between the dislocation line and the EBSD map plane. The magnitude of l ranges from 1 (when the dislocation line is perpendicular to the EBSD map plane) to 0 (when the dislocation lies within the EBSD map plane).

We applied the point-by-point WBV calculations (Wheeler et al., 2009) on the EBSD maps with 5 μm step size. The WBV magnitude of each pixel ($\|\mathbf{WBV}\|$), which provides a minimum estimation for the magnitude of dislocation density tensor, was calculated from the Euclidean norm of the WBV. The sub-grain boundaries were defined at where the $\|\mathbf{WBV}\|$ is higher than $0.0026 \mu\text{m}^{-1}$. This threshold for defining subgrain boundaries is equivalent to a misorientation of 0.75° , which is higher than the limit of angular error of EBSD data. We calculated the c -component WBV (WBV_c) of the pixels on the sub-grain boundaries (Chauve et al., 2017). The proportion of c -component WBV (ϕ_{WBV_c}) was quantified from the ratio between $|\text{WBV}_c|$ and $\|\mathbf{WBV}\|$. The value of ϕ_{WBV_c} ranges from 0 (when the dislocation is dominated by a -component Burgers vectors) to 1 (when the dislocation is dominated by c -component Burgers vectors).

The EBSD maps with 5 μm and 30 μm step size have been used to generate the crystallographic preferred orientation (CPO) data with one point per pixel. The CPO data were contoured with a half-width of 7.5° based on the maximum of multiples of a uniform distribution (MUD) of the points, for a better recognition of the CPO pattern. The MUD value is higher at the orientation that contains a higher density of points. The CPO intensity was quantified by the M-index (Skemer et al., 2005). The M-indices and eigenvalues are consistent between CPOs generated from the EBSD maps with 30 μm and 5 μm step sizes. The CPOs of ice deformed under uniaxial compression at high temperatures are often characterised by c -axes aligning in an open cone (i.e., small circle) (Fig. 1(a)), around the compression axis (Kamb, 1972; Jacka and Maccagnan, 1984; Wilson et al., 2014; Jacka and Li, 2000; Qi et al., 2017). In order to quantify cone opening-angles, we counted the number of c -axes that lie at a given angle (“co-latitude”) from the compression axis (method adapted from Jacka and Maccagnan, 1984, and Piazzolo et al 2013). In practice we counted the c -axes between two co-latitudes separated by a 4° interval (selected by trial, see section



S1 of the supplementary material for the sensitivity test of co-latitude range) and calculated the MUD for this co-latitude range to plot on a graph of MUD as a function of co-latitude (Fig. 1).

3 Results

3.1 Mechanical data

5 The stress-strain curves for all the deformed ice samples are plotted in Fig. 2. Imposed initial strain rate and temperature are shown in Table 1 together with peak and final stresses and corresponding strain rates. The strain rate increases slightly with strain (Table 1) as is required for a shortening sample at constant displacement rate. For all the deformation runs, stress initially increases as a function of strain, before reaching the “peak stress” at axial strains of $0.01 \leq \varepsilon \leq 0.04$. Beyond the peak stress, stress decreases with increasing strain, with the rate of stress drop decreasing with increasing strain. At strains larger than ~ 0.1 ,
10 stresses reduce only a modest amount, with steady-state reached at a strain of ~ 0.2 . Peak and final stresses are larger at colder temperatures and the peak stresses are better defined at $-30\text{ }^{\circ}\text{C}$ than at the warmer temperatures.

3.2 Microstructure

EBSD data are used to generate the illustrative grain orientation maps, grain sub-structure maps, as highlighted by WBV analysis, grain size distributions and subgrain size distributions shown in Fig. 3-5. The grain size and subgrain size distributions
15 are presented as histograms with $4\text{ }\mu\text{m}$ bins. The subgrain size distributions are calculated with the boundary misorientation angle, $\varphi \geq 2^{\circ}$. Note that the quantitative microstructural analyses and CPO data are based on larger areas than those presented in the EBSD maps (Table 2).

3.2.1 Sub-structure

Distinct intragranular distortions and sub-grain boundaries can be observed in all the samples (Fig. 3 (c), 4 (c) and 5 (c)).
20 Kinking, which breaks large grains into irregular shapes and sizes, can be observed in samples deformed at $-30\text{ }^{\circ}\text{C}$ to strains higher than $\sim 3\%$. At -20 and $-30\text{ }^{\circ}\text{C}$, samples with strains higher than $\sim 12\%$ show a “core-and-mantle” structure (Gifkins, 1976; White, 1976), which is characterised by a “net” structure formed by finer grains encircling larger grains with slightly curved boundaries.

CPO development, indicated by grain colours in microstructure maps, occurs with increasing strain. At $-10\text{ }^{\circ}\text{C}$, grains with
25 near-pink-and-orange colours dominate the IPF maps (Fig. 3(a-b)) at strains higher than $\sim 8\%$. At -20 and $-30\text{ }^{\circ}\text{C}$, grains with red, pink and orange colours predominant in the IPF maps (Fig. 5(a-b) and 6 (a-b)) at $\sim 20\%$ strain.



3.2.2 Grain size

The undeformed ice samples all exhibit $< 1\%$ porosity and a homogeneous foam-like structure, with a mean grain size of $\sim 230 \mu\text{m}$ (Qi et al., 2017). For all the samples deformed to $\sim 3\%$ strain, the grain size distributions are strongly skewed or possibly bimodal, with the main peak at finer grain sizes and a tail of coarser sizes with secondary peaks including grain sizes
5 corresponding to the mean grain size of starting material (Fig. 3(d), 4(d) and 5(d)). As the strain increases, the grain size generally gets smaller. The range of the grain size distribution generally narrows, with the proportion of finer grains increasing and the coarse grain tail shortening (Fig. 3(d), 4(d) and 5(d)).

For each sample, we calculated the mean grain diameter (\bar{D}), the peak grain diameter (D_{peak}) and square mean root diameter ($D_{SMR} = (\sqrt{\bar{D}})^2$), presented in Table 3. While the mean diameter, \bar{D} , is commonly used for grain size analyses in the literature
10 (e.g., Jacka, 1994; Piazzolo et al., 2013; Vaughan et al., 2017; Qi et al., 2017; Qi et al., 2019), Lopez-Sanchez and Llana-Fúnez (2015) showed that the frequency peak (D_{peak}) of a grain size distribution provides the most robust measure of the recrystallized grain size. However, the population of grains smaller than D_{peak} is too small to provide representative CPO information for most of the data sets in this study. Meanwhile, D_{SMR} minimizes the bias from very large grains in the calculation of an average and is therefore better suited than \bar{D} and D_{peak} for separating small and large grain populations.

\bar{D} , D_{SMR} and D_{peak} have the relation of $\bar{D} > D_{SMR} > D_{peak}$, and converge as the strain increases, with \bar{D} and D_{SMR} becoming
15 stable after $\sim 12\%$ strain (Fig. 3 (d), 4 (d), 5(d) and Table 3). For each temperature series, we defined a threshold grain size, equals to the D_{SMR} of the sample deformed to $\sim 12\%$ strain. The grains with the grain sizes greater than the threshold were classified as “big grains”. Grains smaller than or equal to the threshold were classified as “small grains”. The “small grains” are likely include all the recrystallized grains (Lopez-Sanchez and Llana-Fúnez, 2015) and some of the remnant grains. We
20 calculated the mean diameters of “big grains” ($\overline{D_{big}}$) and “small grains” ($\overline{D_{small}}$) for all deformed samples. The evolutions of \bar{D} , $\overline{D_{big}}$ and $\overline{D_{small}}$ as a function of strain at different temperatures are illustrated in Fig. 12(a). \bar{D} generally decreases with strain, and it is lower at colder temperatures relative to higher temperatures for samples deformed to strains higher than $\sim 8\%$. $\overline{D_{small}}$ for each temperature series barely changes with strain, and it is higher at -10°C than at -20 and -30°C . At strains lower than $\sim 12\%$, $\overline{D_{big}}$ generally decreases with strain, and it is larger at warmer temperatures.

3.2.3 Subgrain size

Trimby and others (1998) and Wheeler and others (2003) pointed out that different deformation mechanisms such as recovery, subgrain rotation and grain boundary migration (GBM) can produce identifiable grain boundary hierarchy signatures. Inspired
by these works, we calculated mean subgrain sizes (\bar{d}) by applying $\geq 2^\circ$, $\geq 4^\circ$, $\geq 6^\circ$, $\geq 8^\circ$ boundary misorientations (φ) for all deformed samples (Table 3, Fig. 6).

30 As the boundary misorientation φ decreases, the mean subgrain size (\bar{d}) drops. At each φ , \bar{d} generally gets smaller as the strain increases but the trend is not simple. For each sample, the distribution of subgrain size at boundary misorientation angle $\varphi \geq$



2° (Fig. 3(e), 4(e) and 5(e)) is similar to the grain size distribution (Fig. 3(d), 4(d) and 5(d)), but the main peak in the subgrain size distribution is at a finer size than the main peak of the grain size distribution (Table 3). At lower temperature, the boundary hierarchy distribution has the same shape but at smaller subgrain or grain sizes (Fig. 6). It is worth noticing that the $\overline{D_{small}}$ is closer to \bar{d} at $\varphi \geq 2^\circ$ at $\sim 20\%$ strain as the temperature decreases (Fig. 6). The ratio between mean recrystallized grain size and mean subgrain size has been considered as a useful parameter to quantify the recrystallization mechanism (Halfpenny et al., 2012): because subgrain rotation recrystallization should produce grains that have similar sizes with subgrains, while bulging nucleation should produce grains that have smaller sizes than subgrains (Halfpenny et al., 2012). The “small grains” in this study probably contain all the recrystallized grains and some of the remnant grains. Therefore, $\overline{D_{small}}$ can be considered as a maximum estimate of the mean recrystallized grain size. We calculated the ratio ζ_{diff} ($= \overline{D_{small}}/\bar{d}$) for all deformed samples (Table 3). ζ_{diff} values are between 0.4 and 0.6 at strains up to 8% at -10 and -20 °C. Low strain ζ_{diff} values are slightly higher at -30 °C. At -10 °C, the largest ζ_{diff} of 0.6 is at high strains ($\sim 12\%$ and $\sim 20\%$). ζ_{diff} values are higher (0.8-1.2) at high strains (12% and 20%) at lower temperatures (-20 and -30 °C).

3.2.4 Grain boundary geometry

The microstructures of deformed ice samples are characterised by larger grains interlocking with finer grains. At -10 °C, the boundaries of larger grains are generally more irregular (lobate) (Fig. 3(a) and 3(b)) than the boundaries of larger grains at -30 °C (Fig. 5(a) and 5(b)). Quantification of grain boundary lobateness has been considered as a useful microstructural parameter (Krul and Nega, 1996; Takahashi et al., 1998) to infer processes and to correlate with deformation conditions. In this study, we quantified the boundary shape of each ice grain by introducing a sphericity parameter Ψ , which is calculated from grain area A , grain boundary perimeter P and grain radius R . Ψ is defined as:

$$\Psi = \frac{A}{P \times R} \quad (3)$$

The sphericity parameter Ψ can be considered as a useful indicator for grain boundary lobateness because Ψ measures how closely the ice grain boundary shape resembles that of a perfect circle. Ψ decreases from 0.5, where the grain has a perfect round shape, to 0, where the grain is infinitely serrated. Examples of grains and specific geometric shapes that present different Ψ values are illustrated in Fig. 7. This method is similar to that applied by Takahashi and others (1998) to quantify grain boundary shapes. We plotted the Ψ values as a function of grain sizes for all deformed samples grouped by deformation temperature and strain (Fig. 8). At any given temperature and strain, there is an inverse relationship between Ψ and grain size, indicating that “big grains” are generally more lobate than “small grains”. As strain increases, the lobateness of “small grains” remains more-or-less constant, while “big grains” become more lobate and shift to progressively lower values of Ψ . Thus, the grain boundary lobateness of “small” and “big” grains become more distinct with increasing strain. As temperature increases, Ψ decreases more rapidly with increasing grain size, and “big grains” evolve to smaller values of Ψ , reflecting an overall increase in grain boundary lobateness of “big grains” with increasing temperature.



3.3 Crystallographic preferred orientations

The contoured c -, a - and m -axes pole figures are illustrated in Fig. 9-11. The contoured pole figures are presented with (1) the compression axis vertical and (2) with the compression axis perpendicular to the page. These two reference frames, which are commonly used by different communities, enable different elements of symmetry to be illustrated. We calculated the M-indices for the three grain size categories, including “all grains”, “big grains” and “small grains” from the EBSD maps with 5 μm step size (Fig. 12(b)). The M-indices for all grains are consistent between CPOs generated from the EBSD pixel maps with 30 μm and 5 μm step sizes (Table 2): small grains cannot be separated robustly in the 30 μm data sets. The undeformed ice samples exhibit a random CPO with the M-index of 0.0026 (Qi et al., 2017). For all the deformed samples, the M-indices of “big grains” present a similar evolution pattern to “all grains” as the strain increases. The “small grains” generally exhibit lower M-indices at strains of $\varepsilon \geq \sim 5\%$. To illustrate the CPO differences between “big grains” and “small grains”, we present the contoured c -axes CPOs for both big and small grains for the samples deformed to $\sim 12\%$ strain (Fig. 13). The “big grains” and “small grains” have similar patterns of c -axes CPOs. At -10°C , the CPO intensity of “small grains” is lower than “big grains”, and this contrast becomes strengthened as the temperature decreases.

3.3.1 -10°C series

The CPO of the sample (PIL176) deformed to $\sim 3\%$ strain at -10°C is characterized by several weak maxima of c -axes with similar angles relative to the compression direction, and random distributions of a - and m -axes. As the strain increases from $\sim 5\%$, the CPO becomes clearer, with c -axes aligned in a cone (small circle), and the a - and m -axes align in a broad swath along the plane perpendicular to the compression axis and bound by the c -axis cone. The opening-angle θ of the c -axis cone decreases with strain, from $\sim 40^\circ$ at $\sim 5\%$ strain to $\sim 34^\circ$ at $\sim 20\%$ strain. CPO intensity rises with strain in all grain size categories. At $\sim 12\%$ strain, the c -axes of “big grains” align in interconnected elongated maxima that form a cone. The “small grains” exhibit a slightly weaker c -axis CPO, which is characterised by an overall cone of overlapping distinct maxima.

3.3.2 -20°C series

The CPO of the sample (PIL183) deformed to $\sim 3\%$ strain at -20°C is approximately random. At $\sim 5\%$ strain (PIL182), the CPO is characterized by a blurred cone formed by several weak maxima of c -axes, and randomly distributed a - and m -axes. As the strain increases from $\sim 8\%$ to $\sim 12\%$, the CPO becomes clearer, with c -axes aligned in distinct clusters superposed on a blurred broad cone. The a - and m -axes align in weak a broad swath along the plane perpendicular to the compression axis and bound by the c -axis small cone. At $\sim 20\%$ strain, the c -axes align in a cone (small circle), and the a - and m -axes align in broad swath along the plane perpendicular to the compression axis and bound by the c -axis small cone. The opening-angle θ of the c -axes cone is $\sim 29 \pm 3^\circ$ and showing no clear pattern with strain. CPO intensity increases with strain for all grain size categories. At $\sim 12\%$ strain, the c -axes of “big grains” align in distinct maxima superposed on a blurred cone. The “small grains” exhibit a much weaker c -axis CPO, which is characterised by a blurred broad cone with overlapping weak maxima.



3.3.3 -30 °C series

The CPOs of the samples (PIL165, PIL162) deformed to ~3% and ~5% strain at -30 °C are approximately random. As the strain increases from ~8% to ~12%, the *c*-axis CPO exhibits a pattern of a distinct narrow cone superposed on an overall broad cluster, the *a*- and *m*-axes align in a broad swath along the plane perpendicular to the compression axis. At ~20% strain, the *c*-axes align in distinct clusters superposed on an overall broad cluster, and the *a*- and *m*-axes align in a broad swath along the plane perpendicular to the compression axis and bound by the *c*-axis narrow cone. The opening-angle θ of the *c*-axes cone is ~15±1° at ~8% and ~12% strain, and it decreases to ~8° at ~20% strain. CPO intensity increases mildly with strain for “all grains” and “big grains”. For “small grains” the CPO intensity remains at similar values to the starting material before ~12% strain, and it increases slightly at ~20% strain. At ~12% strain, the *c*-axes of “big grains” align in distinct maxima superposed on a blurred broad cluster. The “small grains” exhibit a significantly weaker *c*-axis CPO, which is characterised by a blurred broad cone with overlapping weak and blurred maxima.

3.4 The opening-angle of the *c*-axis cone

We compare the evolution of the opening-angle, θ , of the cone-shaped *c*-axis CPO with the results from previous studies (Table 4 and Fig. 14). For data from the literature, we digitised the *c*-axis orientations from published stereonet (Jacka and Maccagnan, 1984; Jacka and Li, 2000) and calculated θ using the same method described in Section two (Method). For data from Montagnat and others (2015) and Craw and others (2018), we measured the values of θ directly from contoured *c*-axis CPO figures. For data from Vaughan and others (2017), we calculated the values of θ from raw EBSD data. The values of θ for samples from Piazzolo and others (2013) and Qi and others (2017) are taken directly from these papers. The experiments reported by Piazzolo and others (2013) were conducted on D₂O ice at -7 °C, which is a direct analogue for deforming H₂O ice at -10 °C (Wilson et al., 2019). These angles were analysed using methods similar to ours. In order to make a direct comparison with the data reported from this study and Qi and others (2017), we converted the reported axial engineering strain (*e*) and strain rate (\dot{e}) (Piazzolo et al., 2013; Montagnat et al., 2015; Vaughan et al., 2017) to true axial strain (ε) and strain rate ($\dot{\varepsilon}$) using the equations:

$$\varepsilon = -\ln(1 - e) \quad (4)$$

$$\dot{\varepsilon} = \frac{\dot{e}}{1 - e} \quad (5)$$

Equation (6) and (7) were used to forward model axial engineering strain (*e*) and strain rate (\dot{e}) from octahedral shear strain (γ) and strain rate ($\dot{\gamma}$) (Jacka and Maccagnan, 1984; Jacka and Li, 2000).

$$\gamma = \frac{\sqrt{2}}{3} \left(e + \frac{1}{\sqrt{1 - e}} - 1 \right) \quad (6)$$

$$\dot{\gamma} = \frac{\sqrt{2}}{3} \left(\frac{1}{2(1 - e)^{\frac{3}{2}}} + 1 \right) \dot{e} \quad (7)$$



After that, the axial engineering strain (e) and strain rate (\dot{e}) were converted to true axial strain (ϵ) and strain rate ($\dot{\epsilon}$) using Eq. (4) and Eq. (5). The derivation of Eq. (4-7) are shown in section S2 of the supplementary material.

To our knowledge, Fig. 14 contains data from all published 3-D uniaxial compression ice experiments that present c -axis CPOs as a function of strain. 2-D experiments, involving deformation on a microscope stage (e.g. Peternell et al., 2014; Peternell and Wilson, 2016) are excluded as these have different kinematics. There are numerous other high temperature and low strain rate axial compression experiments to strains of ~10% to 30% where c -axis cones have opening-angles of ~35 degrees (e.g., Wilson and Russell-Head, 1982; Gao and Jacka, 1987; Treverrow et al., 2012; Wilson et al., 2019). These data are consistent with the pattern shown in Fig. 14 but are not part of a strain series and are not added to the diagram to maintain clarity. There are comparatively few CPOs from samples at low temperatures (< -15 °C) so we have included all published data from experiments at < -15 °C irrespective of whether these are part of a strain series. The values of θ are scattered between 0° and 42° for all experiments. Experiments to low strains have random CPOs where a cone angle cannot be defined, and these data are not shown on Fig. 14. The evolution pattern of θ as a function of strain at temperatures warmer than -15 °C show θ decreases with increasing strain up to ~20% true axial strain. The only two data points of θ from samples deformed to the strain of ~50% are at 30° . There is little difference as a function of temperature at ≥ -15 °C.

Samples deformed at temperatures colder than -20 °C have lower θ values compared with samples deformed at warmer temperatures at similar strains. At -30 °C, the opening-angle of the c -axis cone decreases to $\sim 0^\circ$ at strains of ~20%. The strain corresponding to the formation of a clear c -axis cone (non-random CPO) increases with decreasing temperature.

4 Discussion

4.1 Deformation mechanism

4.1.1 Inferences from mechanical evolution

The stress-strain curves (Fig. 1) at all temperatures first rise to the peak stresses and then relax to approach near-constant stresses with strains. This pattern matches published constant-displacement-rate experiments (Mellor and Cole, 1982; Durham et al., 1983; Durham et al., 1992; Piazzolo et al., 2013; Vaughan et al., 2017; Qi et al., 2017; Craw et al., 2018; Qi et al., 2019), and is comparable to the constant-load experiments (Budd and Jacka, 1989; Jacka and Li, 2000; Treverrow et al, 2012; Wilson and Peternell, 2012) where strain rate first decreases to a minimum and then increases to approach a near-constant strain rate. Much of the stress increase prior to peak stress relates to elastic strain. However, linear portions have slopes of ~1GPa and this is below the published value of Young's modulus (~9GPa: Gammon et al, 1983). This and the curvature of the stress strain line at the start of each experiment suggests that there is also some dissipative deformation here. This can include porosity loss (Vaughan et al., 2017) and the intergranular stress redistribution used to explain primary creep in constant load experiments (Duval et al, 1983). The drop of stress after peak correlates with dynamic recrystallization driven grain size reduction and CPO development (Jacka and Maccagnan, 1984; Vaughan et al., 2017; Qi et al., 2019). Experiments with initial grain size as a



variable, under comparable conditions to our experiments, suggest that grain size sensitive mechanisms are important (Qi et al., 2017). Grain boundary sliding (GBS) is kinematically required for all grain size sensitive mechanisms (Stevens, 1971; Gates and Stevens, 1974), including diffusion creep (Boullier and Gueguen, 1975; Behrmann and Mainprice, 1987) and dislocation slide accompanied by GBS (disGBS) (Warren and Hirth, 2006). Goldsby and Kohlstedt (1997, 2001, 2002) suggest a general importance of GBS on the basis of the constitutive law parameters required to fit the mechanical data from experimentally deformed fine-grained ice. Recent studies suggest GBS in fine-grained ice layers has a key role in controlling the Greenland ice flow (Kuiper et al., 2019a, 2019b) by applying the Goldsby-Kohlstedt flow law (Goldsby and Kohlstedt, 1997, 2001) to modelling the deformation in the NEEM (North Greenland Eemian Ice Drilling) deep ice core. The grain size reduction resulting from dynamic recrystallization is thought to cause mechanical weakening by increasing the strain rate contribution of grain size sensitive deformation mechanisms (De Bresser et al., 2001). A development of strong CPO can also lead to mechanical weakening in viscously anisotropic materials (Durham and Goetze, 1977; Hansen et al., 2012) such as ice. Our experiments show higher peak and steady-state stress values at colder temperatures than at warmer temperatures. This phenomenon is well known, and the temperature dependence of creep rate is commonly parameterised using an Arrhenius relationship with an activation enthalpy (sometimes called entropy) (Homer and Glen, 1978; Durham et al., 1983, 2010; Cuffey & Paterson, 2010; Scapozza & Bartlett, 2003).

4.1.2 Inferences from grain size distribution and microstructure

For all the deformed samples, the grain size distributions are characterised by peaks at finer grain sizes, and a smaller mean grain size compared with the undeformed sample. These observations suggest that nucleation, which generates grains with smaller sizes, is involved in the dynamic recrystallization processes. Microstructure maps and WBV analyses show subgrain boundaries in all deformed samples (Fig. 3(a-c), 4(a-c) and 5(a-c)). Moreover, the plots of mean subgrain size (\bar{d}) as a function of boundary misorientation angle (φ) for all samples (Fig. 6) show \bar{d} drops with decreasing φ , indicating a development of continuous boundary hierarchy (Trimby et al., 1998). Study in deformed quartz mylonites infer that a continuous boundary hierarchy development with φ can be correlated with a simultaneous operation of recovery and subgrain rotation (Trimby et al., 1998). Therefore, we infer the recovery and subgrain rotation were active in all deformed samples.

At -10 °C, the distribution of grain sphericity parameter Ψ for “big grains” reduces with increasing strain (Fig. 8(a)), and the IQRs of Ψ values for “big grains” show lower median point values at larger grain sizes at strains higher than ~5% (Fig. 8(b)). These phenomena suggest the larger grains become more lobate with strain, indicating a continuous operation of strain-induced grain boundary migration (GBM) (Urai et al., 1986) with increasing strain. At -20 and -30 °C, the IQRs of Ψ values for “big grains” show a stabilisation of median points at ~0.35 at strains lower than ~12% (Fig. 8 (d) and (f)), suggesting many of the “big grains” are of low lobateness. This makes sense as GBM is thermally activated (Merkle et al., 2004), and it should be less active when temperature drops (Urai et al., 1986; Piazzolo, et al., 2006). At lower temperature, the boundary hierarchy distribution has the same shape but at smaller subgrain or grain sizes (Fig. 6). This is likely a consequence of the higher stresses



of the lower temperature experiments resulting in smaller subgrain and recrystallised grain sizes through a piezometer or similar relationship.

At -10 °C, the ratios (ζ_{diff}) between the mean grain sizes of “small grains” ($\overline{D_{small}}$) and mean subgrain sizes (\bar{d}) at boundary misorientation angle (φ) higher than 2° are lower than or equal to 0.6 (Table 3). This phenomenon suggests the “small grains” are smaller than subgrains. However, at lower temperatures, the ζ_{diff} values are higher, indicating that the grain sizes of “small grains” and subgrains become similar at lower temperatures. Comparing recrystallized and subgrain size has been used to discriminate nucleation mechanisms, including subgrain rotation recrystallization and bulging (Halfpenny et al., 2006; Halfpenny et al., 2012; Platt and De Bresser, 2017). The ζ_{diff} provides a maximum estimation of the ratio between recrystallized grains and subgrains because the “small grains” used for the calculation probably contain all of the recrystallized grains and some of the remnant grains. Subgrain rotation is a process that involves an increase in the misorientation across the subgrain boundary resulting from continuous addition of dislocations (Lallemant, 1985; Placidi et al., 2004). New grains will form as the misorientation across the subgrain boundary becomes large enough, with the subgrain boundary eventually dividing its parent grain (Poirier and Nicolas, 1975; Guillope and Poirier, 1979; Urai et al., 1986; Gomez-Rivas et al., 2017). This process is known as the subgrain rotation recrystallization (Hirth and Tullis, 1992; Stipp et al., 2002; Passchier and Trouw, 2005). When subgrain rotation recrystallization is responsible for the nucleation, the recrystallized daughter grains should be initially of a similar size to the internal subgrain size of the parent grain (Urai et al., 1986). Our data show the “small grains” are smaller than subgrains for all samples deformed at -10 °C and samples deformed to lower strains at -20 and -30 °C. This observation suggests subgrain rotation recrystallization alone is unlikely to be the nucleation mechanism. Halfpenny and others (2006, 2012) suggest the bulge nucleation is important in facilitating recrystallization during strain-induced GBM, based on the observation of smaller bulges compared with subgrains in deformed quartz mylonite. The size of the bulge is not controlled by the subgrain size because the bulge can be achieved by the development of a bridging subgrain boundary across the neck of the bulge and its conversion by progressive misorientation into a high-angle grain boundary (Urai et al., 1986). Therefore, we suggest a larger subgrain size compared with the grain size of “small grains” should result from the activation of bulge nucleation in samples deformed at -10 °C. The bulging in this case is a consequence of strain-induced GBM that is favored by high boundary mobility at higher temperatures. The ratios (ζ_{diff}) between the mean grain sizes of “small grains” and mean subgrain sizes suggest that bulging becomes less important at -20 and -30 °C (Table 3). At -20 and -30 °C, network of smaller grains encircles bigger grains at strains higher than 12%. Previous studies on deformed metals and quartzites describe the structure of smaller grains encircling larger grains as “core-and-mantle” structure (Gifkins, 1976; White, 1976). The production of smaller grains that form the “mantle” region was considered as a result of continual rotation of subgrains to develop small strain free grains (White, 1976; Jacka and Li, 2000). Therefore, we suggest the subgrain rotation recrystallization alone is the dominate nucleation mechanism at -20 and -30 °C.



4.1.3 Inferences from the CPO development

The CPO intensity and opening-angle of the *c*-axis CPO decrease as the temperature drops. Previous studies suggest the CPO development is mainly controlled by the deformation and recrystallization mechanisms (Alley, 1992; Qi et al., 2017). Fig. 15 explains how key processes (Fig. 15(b)) involved in the deformation and recrystallization mechanisms (Fig. 15(a)) may affect the CPO development as a function of strain and temperature (Fig. 15(c)).

At -10 °C, the prevalence of larger grains with lobate grain boundaries and the increase in lobateness with grain size and with strain (as indicated by parameter Ψ), suggest that strain-induced GBM is an important process. Our -10 °C series CPO data show a continuous enhancement of CPO intensity as indicated by M-index, and a clearer cone-shaped pattern of the *c*-axes with increasing strain. Similar phenomena have been observed in previous ice deformation experiments, and they were used to infer that the strain-induced GBM favours the growth of grains with easy slip orientations (Vaughan et al., 2017; Qi et al., 2017). Because grains with hard slip orientations should have greater internal distortions (Bestmann and Prior 2003), and therefore store higher internal strain energy, they are likely to be consumed by grains with easy slip orientations through GBM (Piazolo et al., 2006; Killian et al., 2011; Qi et al., 2017; Xia et al., 2018). The cone opening-angles θ for samples deformed at -10 °C decrease from 40° at ~5% strain to 34° at ~20% strain, rather than stabilise at the easiest slip orientation of 45°. This observation suggests GBM alone cannot be the mechanism that controls the CPO development. The narrowing of cone-shaped *c*-axis CPO has been explained by an activation of grain rotation (Vaughan et al., 2017; Qi et al., 2017). Similarly, we infer the decreasing of opening-angle θ as a function of strain is likely to result from an acceleration in the rate of grain rotation driven by intracrystalline glide on the basal plane. The observation of subgrains and the continuous boundary hierarchies suggest that recovery and subgrain rotation operated in parallel with strain-induced GBM. The dislocation activity required to generate subgrain structures and to provide the strain energy driving force for strain-induced GBM is likely the primary control on grain rotation (Duval and Castelnau, 1995; Llorens et al., 2016). The CPO intensity (as indicated by M-index) of “small grains” is generally lower than “larger grains” (Fig. 12 (b)). At ~12% strain, both “big grains” and “small grains” develop cone-shaped *c*-axis CPO, but the *c*-axes cone is slightly clearer for “big grains”. These observations suggest a mechanism that weakens the CPO development may be involved in the deformation of “small grains”. Ice deformation experiments applied under comparable conditions suggest that grain size sensitive mechanisms are important in samples deformed at -10 °C (Qi et al., 2017). Previous rock and ice deformation studies reported small recrystallized grains have CPOs that are randomly dispersed equivalents of the stronger host-grain CPOs (Jiang et al., 2000; Bestmann and Prior, 2003; Storey and Prior, 2005; Warren and Hirth, 2006; Craw et al., 2018). These observations are interpreted as the result of an increase in the contribution of GBS in fine grains. Therefore, we infer GBS, a grain size sensitive mechanism, may be more active in “smaller grains”.

“Big grains” are less lobate at lower temperatures, indicating a less effective strain-induced grain boundary migration (GBM). The CPO data suggest the opening-angle θ of the *c*-axes cone as well as the CPO intensity decrease with decreasing temperature. We infer the selective growth of the grains oriented for easy slip orientations becomes less active due to the reduction of GBM activity. Consequently, grain rotation, driven by intracrystalline glide on the basal plane, becomes more



prominent. The less effective GBM together with the more active grain rotation can lead to a closure of c -axis cone at lower temperatures. Microstructural data show bands formed by finer grains that encircle larger grains are better developed at colder temperatures. “Small grains” that contain all recrystallized grains and part of the remnant grains have a lower CPO intensity than “big grains”, and this contrast strengthens from -20 to -30°C (Fig. 13). These phenomena suggest that the overall CPO
5 weakening at lower temperatures corresponds to CPO weakening in “small grains”. Craw and others (2018) reported similar observations in uniaxially deformed Antarctic ice, and the reduction of CPO intensity in grains with finer sizes was attributed to GBS. Similarly, we suggest the grain size sensitivity of GBS (Goldsby and Kohlstedt, 1997; Goldsby and Kohlstedt, 2001) favours a faster strain rate in “small grains” relative to large grains.

4.2 Some thoughts on weakening/enhancement mechanisms

10 All experiments show weakening from peak stress to steady-state stress that correlates with CPO and microstructural development. At -10 °C the CPO developed includes many grains with basal plane orientations that would facilitate further axial shortening and it is intuitive that the CPO development could provide a cause for the weakening. However, at -30 °C the CPO developed at steady-state stress is a cluster with many basal planes sub-perpendicular to compression. In this case the CPO would hinder further axial shortening and it is intuitive that the CPO should cause strengthening. Nevertheless, weakening
15 occurs at -30 °C. Development of CPO cannot provide a uniform explanation for weakening across the range of laboratory experiments presented here. In all cases grain sizes are reduced during deformation. The weakening associated with the increased strain rate contribution of grain size sensitive mechanisms as grain sizes reduce could provide a uniform explanation for weakening across the range of laboratory experiments presented here. This is a topic requiring significant further analysis.

5 Conclusions

- 20
1. We deformed isotropic polycrystalline pure water ice to successive strains (~3%, 5%, 8%, 12% and 20%) under constant displacement rate (strain rate $\sim 1.0 \times 10^{-5} \text{ s}^{-1}$) at -10, -20 and -30 °C. Microstructural and CPO analyses were conducted on deformed ice samples using cryo-EBSD.
 2. In all samples stress rises to a peak stress at ~ 1 to 3% strain and then drops to a lower steady-state stress. Samples deformed at colder temperatures show higher peak and steady-state stresses, as expected for the temperature dependency
25 of creep.
 3. Distinct sub-grain boundaries are observed in all deformed samples and mean subgrain size (\bar{d}) decreases with decreasing boundary misorientation threshold angle (φ). These observations suggest recovery and subgrain rotation were active in all deformed samples. The mean subgrain size at the same boundary misorientation angle drops with decreasing temperature.



4. All deformed samples have skewed grain size distributions with a strong peak at small ($<100\ \mu\text{m}$) sizes and a tail to larger sizes. The peak and mean grain sizes are small compared to undeformed samples ($230\ \mu\text{m}$), suggesting nucleation is involved in dynamic recrystallization processes.
5. For each temperature series, we separated populations of “small grains” and “big grains”. The “small grains” are smaller than subgrains for all samples deformed at $-10\ ^\circ\text{C}$. “Small grains” and subgrains are similar in size at -20 and $-30\ ^\circ\text{C}$. These observations suggest bulge nucleation facilitates the recrystallization process at warmer temperature, and it becomes less important at colder temperatures. “Core-and-mantle” structure are clearer at -20 and $-30\ ^\circ\text{C}$, suggesting greater activity of subgrain rotation recrystallization.
6. For all deformed samples, “big grains” are more lobate than “small grains”. “Big grains” become more lobate with increasing grain size and with strain at $-10\ ^\circ\text{C}$. The lobateness of “big grains” is close to constant across the grain size range at low strains at $-20\ ^\circ\text{C}$ and at all strains at $-30\ ^\circ\text{C}$. These observations suggest grain boundary migration (GBM) is more prominent at warmer temperatures.
7. Many of the deformed samples have CPOs defined by open cones (small circles) of c -axes. At $-10\ ^\circ\text{C}$, CPO intensity and the definition of the c -axis cone increase as the strain increases, suggesting strain-induced GBM favours the growth of grains at easy slip orientations. The opening-angle of the cone decreases with strain, suggesting strain-induced GBM is balanced by grain rotation facilitated by basal slip as the strain increases. The CPO intensity and opening-angle of the c -axis CPO decrease as the temperature drops from $-10\ ^\circ\text{C}$ to $-30\ ^\circ\text{C}$. The closure of c -axes cone at $-30\ ^\circ\text{C}$ is interpreted as the result of a more active grain rotation together with a less effective GBM. The overall CPO weakening with decreasing temperature correlates with CPO weakening in “small grains”. We suggest grain boundary sliding (GBS), a grain size sensitive mechanism, becomes more important at colder temperatures.
8. Weakening (enhancement) cannot be uniformly caused by CPO development. It is likely that grain size reduction plays a significant role in weakening.

Author contributions. DJP, DLG and SF designed the research. DJP, SF, TH, AJC and CQ performed experiments. SF, DJP and MN collected the cryo-EBSD data. SF, DJP and JW analysed data. SF and DJP wrote the draft. All authors edited the paper.

Acknowledgements. We are thankful to Pat Langhorne for providing the cold room facility at University of Otago. This work was supported by a NASA fund (NNX15AM69G) and two Marsden Funds of the Royal Society of New Zealand (UOO1116 and UOO052). SF was supported by the University of Otago doctoral scholarship, the Antarctica New Zealand doctoral scholarship and the University of Otago PERT (Polar Environment Research Theme) seed funding.

Competing interests. The authors declare that they have no conflict of interest.

Data availability. Data available on request from the authors.



References

- Alley, R. B.: Flow-law hypotheses for ice-sheet modeling, *J. Glaciol.*, 38, 245–256, <https://doi.org/10.1017/s002214300003658>, 1992.
- Alley, R. B., Gow, A. J., and Meese, D. A.: Mapping c-axis fabrics to study physical processes in ice, *Journal of Glaciology*, 5 41, 197-203, <https://doi.org/10.1017/s0022143000017895>, 1995.
- Ashby, M. F.: The deformation of plastically non-homogeneous materials, *The Philosophical Magazine: A Journal of Theoretical Experimental and Applied Physics*, 21, 399-424, <https://doi.org/10.1080/14786437008238426>, 1970.
- Bachmann, F., Hielscher, R., and Schaeben, H.: Grain detection from 2d and 3d EBSD data—Specification of the MTEX algorithm, *Ultramicroscopy*, 111, 1720-1733, <https://doi.org/10.1016/j.ultramic.2011.08.002>, 2011.
- 10 Bamber, J. L., Oppenheimer, M., Kopp, R. E., Aspinall, W. P., and Cooke, R. M.: Ice sheet contributions to future sea-level rise from structured expert judgment, *Proceedings of the National Academy of Sciences of the United States of America*, 116, 11195-11200, <https://doi.org/10.1073/pnas.1817205116>, 2019.
- Behrmann, J. H. and Mainprice, D.: Deformation mechanisms in a high-temperature quartz-feldspar mylonite: evidence for superplastic flow in the lower continental crust, *Tectonophysics*, 140, 297-305, [https://doi.org/10.1016/0040-](https://doi.org/10.1016/0040-1951(87)90236-8)
15 [1951\(87\)90236-8](https://doi.org/10.1016/0040-1951(87)90236-8), 1987.
- Bestmann, M. and Prior, D. J.: Intragranular dynamic recrystallization in naturally deformed calcite marble: diffusion accommodated grain boundary sliding as a result of subgrain rotation recrystallization, *Journal of Structural Geology*, 25, 1597-1613, [https://doi.org/10.1016/s0191-8141\(03\)00006-3](https://doi.org/10.1016/s0191-8141(03)00006-3), 2003.
- Bindschadler, R. A., Nowicki, S., Abe-Ouchi, A., Aschwanden, A., Choi, H., Fastook, J., Granzow, G., Greve, R., Gutowski, 20 G., Herzfeld, U., Jackson, C., Johnson, J., Khroulev, C., Levermann, A., Lipscomb, W. H., Martin, M. A., Morlighem, M., Parizek, B. R., Pollard, D., Price, S. F., Ren, D. D., Saito, F., Sato, T., Seddik, H., Seroussi, H., Takahashi, K., Walker, R., and Wang, W. L.: Ice-sheet model sensitivities to environmental forcing and their use in projecting future sea level (the SeaRISE project), *Journal of Glaciology*, 59, 195-224, <https://doi.org/10.3189/2013jog12j125>, 2013.
- Boullier, A. M. and Gueguen, Y.: SP-mylonites: origin of some mylonites by superplastic flow, *Contributions to Mineralogy and Petrology*, 50, 93-104, <https://doi.org/10.1007/bf00373329>, 1975.
- 25 Budd, W. F. and Jacka, T. H.: A review of ice rheology for ice sheet modelling, *Cold Regions Science and Technology*, 16, 107-144, [https://doi.org/10.1016/0165-232x\(89\)90014-1](https://doi.org/10.1016/0165-232x(89)90014-1), 1989.
- Chauve, T., Montagnat, M., Piazzolo, S., Journaux, B., Wheeler, J., Barou, F., Mainprice, D., and Tommasi, A.: Non-basal dislocations should be accounted for in simulating ice mass flow, *Earth and Planetary Science Letters*, 473, 247-255, 30 <https://doi.org/10.1016/j.epsl.2017.06.020>, 2017.
- Craw, L., Qi, C., Prior, D. J., Goldsby, D. L., and Kim, D.: Mechanics and microstructure of deformed natural anisotropic ice, *J. Struct. Geol.*, 115, 152–166, <https://doi.org/10.1016/j.jsg.2018.07.014>, 2018.



- Cole, D. M.: Preparation of polycrystalline ice specimens for laboratory experiments, *Cold Regions Science and Technology*, 1, 153-159, [https://doi.org/10.1016/0165-232x\(79\)90007-7](https://doi.org/10.1016/0165-232x(79)90007-7), 1979.
- Cuffey, K.M. and Paterson, W.S.B. (4th Eds.): *The Physics of Glaciers*, Butterworth-Heinemann, Elsevier, U.S.A., 2010.
- De Bresser, J., Ter Heege, J., and Spiers, C.: Grain size reduction by dynamic recrystallization: can it result in major rheological
5 weakening?, *Int. J. Earth Sci.*, 90, 28–45, <https://doi.org/10.1007/s005310000149>, 2001.
- Dutton, A., Carlson, A. E., Long, A. J., Milne, G. A., Clark, P. U., DeConto, R., Horton, B. P., Rahmstorf, S., and Raymo, M. E.: Sea-level rise due to polar ice-sheet mass loss during past warm periods, *Science*, 349, 153, <https://doi.org/10.1126/science.aaa4019>, 2015.
- Durham, W. B. and Goetze, C.: Plastic flow of oriented single crystals of olivine: 1. Mechanical data, *Journal of Geophysical
10 Research*, 82, 5737-5753, <https://doi.org/10.1029/jb082i036p05737>, 1977.
- Durham, W. B., Heard, H. C., and Kirby, S. H.: Experimental deformation of polycrystalline H₂O ice at high pressure and low temperature: Preliminary results, *Journal of Geophysical Research: Solid Earth*, 88, B377-B392, <https://doi.org/10.1029/jb088is01p0b377>, 1983.
- Durham, W. B., Kirby, S. H., and Stern, L. A.: Effects of dispersed particulates on the rheology of water ice at planetary
15 conditions, *Journal of Geophysical Research: Planets*, 97, 20883-20897, <https://doi.org/10.1029/92je02326>, 1992.
- Durham, W. B., Prieto-Ballesteros, O., Goldsby, D. L., and Kargel, J. S.: Rheological and Thermal Properties of Icy Materials, *Space Science Reviews*, 153, 273-298, <https://doi.org/10.1007/s11214-009-9619-1>, 2010.
- Duval, P., Ashby, M. F., and Anderman, I.: Rate-controlling processes in the creep of polycrystalline ice, *J. Phys. Chem.*, 87, 4066–4074, <https://doi.org/10.1021/j100244a014>, 1983.
- 20 Duval, P. and Castelnau, O.: Dynamic recrystallization of ice in polar ice sheets, *J. Phys. IV*, 05, C3–197–C3–205, <https://doi:10.1051/jp4:1995317>, 1995.
- Faria, S. H., Weikusat, I. and Azuma, N.: The microstructure of polar ice. Part II: State of the art, *Journal of Structural Geology*, 61, 21–49, <https://doi.org/10.1016/j.jsg.2013.11.003>, 2014.
- Gammon, P. H., Kieft, H., Clouter, M. J., and Denner, W. W.: Elastic constants of artificial and natural ice samples by
25 Brillouin spectroscopy, *Journal of glaciology*, 29, 433-460, <https://doi.org/10.3189/s0022143000030355>, 1983.
- Gao, X. Q. and Jacka, T. H.: The approach to similar tertiary creep rates for antarctic core ice and laboratory prepared ice, *J. Phys. Colloques*, 48, C1–289–C1–296, <https://doi:10.1051/jphyscol:1987141>, 1987.
- Gates, R. S., and Stevens, R. N.: Measurement of grain-boundary sliding in polycrystals: *Metallurgical Transactions*, 5, 505-510, <https://doi.org/10.1007/bf02644121>, 1974.
- 30 Gifkins, R.: Grain-boundary sliding and its accommodation during creep and superplasticity, *Metallurgical transactions a*, 7, 1225-1232, <https://doi.org/10.1007/bf02656607>, 1976.
- Goldsby, D. L. and Kohlstedt, D. L.: Grain boundary sliding in fine-grained ice I, *Scripta Materialia*, 37, 1399-1406, [https://doi.org/10.1016/s1359-6462\(97\)00246-7](https://doi.org/10.1016/s1359-6462(97)00246-7), 1997.



- Goldsby, D. L. and Kohlstedt, D. L.: Superplastic deformation of ice: Experimental observations, *Journal of Geophysical Research: Solid Earth*, 106, 11017-11030, <https://doi.org/10.1029/2000jb900336>, 2001.
- Goldsby, D. L. and Kohlstedt, D. L.: Reply to comment by P. Duval and M. Montagnat on “Superplastic deformation of ice: Experimental observations”, *Journal of Geophysical Research: Solid Earth*, 107, ECV-17, <https://doi.org/10.1029/2002jb001842>, 2002.
- 5 Gomez-Rivas, E., Griera, A., Llorens, M. G., Bons, P. D., Lebensohn, R. A., and Piazzolo, S.: Subgrain rotation recrystallization during shearing: insights from full-field numerical simulations of halite polycrystals, *Journal of Geophysical Research: Solid Earth*, 122, 8810-8827, <https://doi.org/10.1002/2017jb014508>, 2017.
- Guillope, M. and Poirier, J. P.: Dynamic recrystallization during creep of single-crystalline halite: An experimental study, *Journal of Geophysical Research: Solid Earth*, 84, 5557-5567, <https://doi.org/10.1029/jb084ib10p05557>, 1979.
- 10 Halfpenny, A., Prior, D. J., and Wheeler, J.: Analysis of dynamic recrystallization and nucleation in a quartzite mylonite, *Tectonophysics*, 427, 3-14, <https://doi.org/10.1016/j.tecto.2006.05.016>, 2006.
- Halfpenny, A., Prior, D. J., and Wheeler, J.: Electron backscatter diffraction analysis to determine the mechanisms that operated during dynamic recrystallisation of quartz-rich rocks, *Journal of Structural Geology*, 36, 2-15, <https://doi.org/10.1016/j.jsg.2012.01.001>, 2012.
- 15 Hansen, L. N., Zimmerman, M. E., and Kohlstedt, D. L.: The influence of microstructure on deformation of olivine in the grain-boundary sliding regime, *J. Geophys. Res.*, 117, B09201, <https://doi.org/10.1029/2012JB009305>, 2012.
- Hartmann, W. K.: Surface evolution of two-component stone / ice bodies in the Jupiter region, *Icarus*, 44, 441-453, [https://doi.org/10.1016/0019-1035\(80\)90036-6](https://doi.org/10.1016/0019-1035(80)90036-6), 1980.
- 20 Heard, H. C., Durham, W. B., Boro, C. O., and Kirby, S. H.: A triaxial deformation apparatus for service at $77 \leq T \leq 273$ K, in: *The Brittle-Ductile Transition in Rocks*, edited by: Duba, A. G., Durham, W. B., Handin, J. W., and Wang, H. F., 225–228, <https://doi.org/10.1029/GM056p0225>, 1990.
- Hirth, G., & Tullis, J.: Dislocation creep regimes in quartz aggregates, *Journal of structural geology*, 14, 145-159, [https://doi.org/10.1016/0191-8141\(92\)90053-y](https://doi.org/10.1016/0191-8141(92)90053-y), 1992.
- 25 Hobbs, B. E., Means, W. D., and Williams, P. F. (1st Eds.): *An outline of structural geology*, Wiley, 1976.
- Homer, D. R. and Glen, J. W.: The creep activation energies of ice, *Journal of Glaciology*, 21, 429-444, <https://doi.org/10.1017/s0022143000033591>, 1978.
- Hudleston, P.J.: Structures and fabrics in glacial ice: a review, *J. Struct. Geol.*, 81, 1–27, <https://doi.org/10.1016/j.jsg.2015.09.003>, 2015.
- 30 Jacka, T. H. and Maccagnan, M.: Ice crystallographic and strain rate changes with strain in compression and extension, *Cold Regions Science and Technology*, 8(3), 269–286, [https://doi.org/10.1016/0165-232x\(84\)90058-2](https://doi.org/10.1016/0165-232x(84)90058-2), 1984.
- Jacka, T. H. and Li, J.: The steady-state crystal size of deforming ice, *Annals of Glaciology*, 20, 13-18, <https://doi.org/10.3189/172756494794587230>, 1994.



- Jacka, T. H. and Li, J.: Flow rates and crystal orientation fabrics in compression of polycrystalline ice at low temperatures and stresses, in: International Symposium on Physics of Ice Core Records, Shikotsukohan, Hokkaido, Japan, 14–17 September 1998, edited by: Hondoh, T., 83–102, 2000.
- Jiang, Z., Prior, D. J., and Wheeler, J.: Albite crystallographic preferred orientation and grain misorientation distribution in a
5 low-grade mylonite: implications for granular flow, *Journal of Structural Geology*, 22, 1663-1674, [https://doi.org/10.1016/s0191-8141\(00\)00079-1](https://doi.org/10.1016/s0191-8141(00)00079-1), 2000.
- Kamb, W. B.: Experimental recrystallization of ice under stress, in: Flow and Fracture of Rocks, edited by Heard, H. C., Borg, I. Y., Carter, N. L., and Rayleigh, C. B., American Geophysical Union, 211–242, <https://doi.org/10.1029/gm016p0211>, 1972.
- 10 Kilian, R., Heilbronner, R., and Stünitz, H.: Quartz grain size reduction in a granitoid rock and the transition from dislocation to diffusion creep, *Journal of Structural Geology*, 33, 1265-1284, <https://doi.org/10.1016/j.jsg.2011.05.004>, 2011.
- Kruhl, J. H. and Nega, M.: The fractal shape of sutured quartz grain boundaries: application as a geothermometer, *Geologische Rundschau*, 85(1), 38-43, <https://doi.org/10.1007/bf00192058>, 1996.
- Kuiper, E. J. N., Weikusat, I., de Bresser, J. H., Jansen, D., Pennock, G. M., and Drury, M. R.: Using a composite flow law to
15 model deformation in the NEEM deep ice core, Greenland: Part 1 the role of grain size and grain size distribution on the deformation of Holocene and glacial ice, *The Cryosphere Discuss*, <https://doi.org/10.5194/tc-2018-275>, 2019a.
- Kuiper, E. J. N., de Bresser, J. H. P., Drury, M. R., Eichler, J., Pennock, G. M. and Weikusat, I.: Using a composite flow law to model deformation in the NEEM deep ice core, Greenland: Part 2 the role of grain size and premelting on ice deformation at high homologous temperature, *The Cryosphere Discussions*, <https://doi.org/10.5194/tc-2018-275>, 2019b.
- 20 Lallemand, H. G. A.: Subgrain rotation and dynamic recrystallization of olivine, upper mantle diapirism, and extension of the Basin-and-Range Province, *Tectonophysics*, 119, 89-117, [https://doi.org/10.1016/0040-1951\(85\)90034-4](https://doi.org/10.1016/0040-1951(85)90034-4), 1985.
- Llorens, M.-G., Griera, A., Bons, P. D., Roessiger, J., Lebensohn, R., Evans, L. and Weikusat, I.: Dynamic recrystallisation of ice aggregates during co-axial viscoplastic deformation: a numerical approach, *Journal of Glaciology*, 62, 1–19, <https://doi.org/10.1017/jog.2016.28>, 2016.
- 25 Lopez-Sanchez, M. A. and Llana-Fúnez, S.: An evaluation of different measures of dynamically recrystallized grain size for paleopiezometry or paleowattometry studies, *Solid Earth*, 6, 475-495, <https://doi.org/10.5194/se-6-475-2015>, 2015.
- Mainprice, D., Bachmann, F., Hielscher, R., and Schaeben, H.: Descriptive tools for the analysis of texture projects with large datasets using MTEX: strength, symmetry and components, *Geological Society, London, Special Publications*, 409, 251-271, <https://doi.org/10.1144/sp409.8>, 2015.
- 30 Mellor, M. and Cole, D. M.: Deformation and failure of ice under constant stress or constant strain-rate, *Cold Regions Science and Technology*, 5, 201-219, [https://doi.org/10.1016/0165-232x\(82\)90015-5](https://doi.org/10.1016/0165-232x(82)90015-5), 1982.
- Merkle, K. L., Thompson, L. J., and Phillipp, F.: In-situ HREM studies of grain boundary migration, *Interface Science*, 12, 277-292, <https://doi.org/10.1023/b:ints.0000028657.72527.5b>, 2004.



- Montagnat, M., Chauve, T., Barou, F., Tommasi, A., Beausir, B., and Fressengeas, C.: Analysis of dynamic recrystallization of ice from EBSD orientation mapping, *Frontiers in Earth Science*, 3, 81, <https://doi.org/10.3389/feart.2015.00081>, 2015.
- Passchier, C. W. and Trouw, R. A. (2nd Eds.): *Microtectonics*, Springer Science & Business Media, 2005.
- Paternell, M., Dierckx, M., Wilson, C. J. L. and Piazzolo, S.: Quantification of the microstructural evolution of polycrystalline fabrics using FAME: Application to in situ deformation of ice, *Journal of Structural Geology*, 61, 109–122, <https://doi.org/10.1016/j.jsg.2013.05.005>, 2014.
- Paternell, M. and Wilson, C. J. L.: Effect of strain rate cycling on microstructures and crystallographic preferred orientation during high-temperature creep, *Geology*, 44, 279–282, <https://doi.org/10.1130/g37521.1>, 2016.
- Piazzolo, S., Bestmann, M., Prior, D. J., and Spiers, C. J.: Temperature dependent grain boundary migration in deformed-then-annealed material: observations from experimentally deformed synthetic rocksalt, *Tectonophysics*, 427, 55-71, <https://doi.org/10.1016/j.tecto.2006.06.007>, 2006.
- Piazzolo, S., Wilson, C. J., Luzin, V., Brouzet, C., and Paternell, M.: Dynamics of ice mass deformation: Linking processes to rheology, texture, and microstructure, *Geochemistry, Geophysics, Geosystems*, 14, 4185-4194, <https://doi.org/10.1002/ggge.20246>, 2013.
- Placidi, L., Faria, S. H., and Hutter, K.: On the role of grain growth, recrystallization and polygonization in a continuum theory for anisotropic ice sheets, *Annals of Glaciology*, 39, 49-52, <https://doi.org/10.3189/172756404781814410>, 2004.
- Platt, J. P. and De Bresser, J. H. P.: Stress dependence of microstructures in experimentally deformed calcite, *Journal of Structural Geology*, 105, 80-87, <https://doi.org/10.1016/j.jsg.2017.10.012>, 2017.
- Poirier, J. P. and Nicolas, A.: Deformation-induced recrystallization due to progressive misorientation of subgrains, with special reference to mantle peridotites, *The Journal of Geology*, 83, 707-720, <https://doi.org/10.1086/628163>, 1975.
- Prior, D.J., Lilly, K., Seidemann, M., Vaughan, M., Becroft, L., Easingwood, R., Diebold, S., Obbard, R., Daghljan, C., Baker, I., and Caswell, T.: Making EBSD on water ice routine, *Journal of microscopy*, 259, 237-256, <https://doi.org/10.1111/jmi.12258>, 2015.
- Qi, C., Goldsby, D. L., and Prior, D. J.: The down-stress transition from cluster to cone fabrics in experimentally deformed ice, *Earth Planet. Sc. Lett.*, 471, 136–147, <https://doi.org/10.1016/j.epsl.2017.05.008>, 2017.
- Qi, C., Prior, D.J., Craw, L., Fan, S., Llorens, M.G., Gricera, A., Negrini, M., Bons, P.D., and Goldsby, D.L.: Crystallographic preferred orientations of ice deformed in direct-shear experiments at low temperatures, *The Cryosphere*, 13, 351-371, <https://doi.org/10.5194/tc-13-351-2019>, 2019.
- Rignot, E., Mouginot, J., and Scheuchl, B.: Ice flow of the Antarctic ice sheet, *Science*, 333, 1427-1430, <https://doi.org/10.1126/science.1208336>, 2011.
- Scapozza, C. and Bartelt, P. A.: The influence of temperature on the small-strain viscous deformation mechanics of snow: a comparison with polycrystalline ice, *Annals of Glaciology*, 37, 90-96, <https://doi.org/10.3189/172756403781815410>, 2003.



- Skemer, P., Katayama, I., Jiang, Z., and Karato, S. I.: The misorientation index: Development of a new method for calculating the strength of lattice-preferred orientation, *Tectonophysics*, 411, 157-167, <https://doi.org/10.1016/j.tecto.2005.08.023>, 2005.
- Stern, L. A., Durham, W. B., and Kirby, S. H.: Grain-size-induced weakening of H₂O ices I and II and associated anisotropic recrystallization, *Journal of Geophysical Research: Solid Earth*, 102, 5313-5325, <https://doi.org/10.1029/96jb03894>, 1997.
- Stevens, R. N.: Grain-boundary sliding and diffusion creep in polycrystalline solids: *Philosophical Magazine*, 23, 265-283, <https://doi.org/10.1080/14786437108216383>, 1971.
- Stipp, M., StüEnitz, H., Heilbronner, R., & Schmid, S. M.: The eastern Tonale fault zone: a ‘natural laboratory’ for crystal plastic deformation of quartz over a temperature range from 250 to 700 C, *Journal of structural geology*, 24, 1861-1884, [https://doi.org/10.1016/s0191-8141\(02\)00035-4](https://doi.org/10.1016/s0191-8141(02)00035-4), 2002.
- Storey, C. D. and Prior, D. J.: Plastic deformation and recrystallization of garnet: a mechanism to facilitate diffusion creep, *Journal of Petrology*, 46, 2593-2613, <https://doi.org/10.1093/petrology/egi067>, 2005.
- Takahashi, M., Nagahama, H., Masuda, T., and Fujimura, A.: Fractal analysis of experimentally, dynamically recrystallized quartz grains and its possible application as a strain rate meter, *Journal of Structural Geology*, 20(2-3), 269-275, [https://doi.org/10.1016/s0191-8141\(97\)00072-2](https://doi.org/10.1016/s0191-8141(97)00072-2), 1998.
- Treverrow, A., Budd, W. F., Jacka, T. H., and Warner, R. C.: The tertiary creep of polycrystalline ice: experimental evidence for stress-dependent levels of strain-rate enhancement, *Journal of Glaciology*, 58, 301-314, <https://doi.org/10.3189/2012jog11j149>, 2012.
- Trimby, P. W., Prior, D. J., and Wheeler, J.: Grain boundary hierarchy development in a quartz mylonite, *Journal of Structural Geology*, 20, 917-935, [https://doi.org/10.1016/s0191-8141\(98\)00026-1](https://doi.org/10.1016/s0191-8141(98)00026-1), 1998.
- Urai, J. L., Means, W. D., and Lister, G. S.: Dynamic recrystallization of minerals, in: *Mineral and Rock Deformation*, edited by: Hobbs, B. and Heard, H., *Laboratory Studies*, 36, 161–199, <https://doi.org/10.1029/gm036p0161>, 1986.
- Vaughan, M. J., Prior, D. J., Jefferd, M., Brantut, N., Mitchell, T. M., and Seidemann, M.: Insights into anisotropy development and weakening of ice from in situ P wave velocity monitoring during laboratory creep, *J. Geophys. Res.-Sol. Ea.*, 122, 7076–7089, <https://doi.org/10.1002/2017JB013964>, 2017.
- Warren, J. M. and Hirth, G.: Grain size sensitive deformation mechanisms in naturally deformed peridotites, *Earth and Planetary Science Letters*, 248, 438-450, <https://doi.org/10.1016/j.epsl.2006.06.006>, 2006.
- Weertman, J.: Creep deformation of ice, *Annual Review of Earth and Planetary Sciences*, 11, 215-240, <https://doi.org/10.1146/annurev.ea.11.050183.001243>, 1983.
- Whalley, W. B. and Azizi, F.: Rock glaciers and protalus landforms: Analogous forms and ice sources on Earth and Mars, *Journal of Geophysical Research: Planets*, 108, <https://doi.org/10.1029/2002je001864>, 2003.
- Wheeler, J., Jiang, Z., Prior, D. J., Tullis, J., Drury, M. R., and Trimby, P. W.: From geometry to dynamics of microstructure: using boundary lengths to quantify boundary misorientations and anisotropy, *Tectonophysics*, 376, 19-35, <https://doi.org/10.1016/j.tecto.2003.08.007>, 2003.



- Wheeler, J., Mariani, E., Piazzolo, S., Prior, D. J., Trimby, P., and Drury, M. R.: The weighted Burgers vector: a new quantity for constraining dislocation densities and types using electron backscatter diffraction on 2D sections through crystalline materials, *Journal of microscopy*, 233, 482-494, <https://doi.org/10.1111/j.1365-2818.2009.03136.x>, 2009.
- White, S.: The effects of strain on the microstructures, fabrics, and deformation mechanisms in quartzites, *Philosophical Transactions of the Royal Society of London, ser. A, Mathematical and Physical Sciences*, 283, 69-86, <https://doi.org/10.1098/rsta.1977.0014>, 1976.
- Wilson, C. J. L. and Russell-Head, D. S.: Steady-state preferred orientation of ice deformed in plane strain at -1° C, *Journal of Glaciology*, 28, 145-160, <https://doi.org/10.3189/s0022143000011850>, 1982.
- Wilson, C. J. and Peternell, M.: Ice deformed in compression and simple shear: control of temperature and initial fabric, *Journal of Glaciology*, 58, 11-22, <https://doi.org/10.3189/2012jog11j065>, 2012.
- Wilson, C. J., Hunter, N. J., Luzin, V., Peternell, M., and Piazzolo, S.: The influence of strain rate and presence of dispersed second phases on the deformation behaviour of polycrystalline D2O ice, *Journal of Glaciology*, 65, 101-122, <https://doi.org/10.1017/jog.2018.100>, 2019.
- Xia, H., & Platt, J. P.: Quartz grainsize evolution during dynamic recrystallization across a natural shear zone boundary, *Journal of Structural Geology*, 109, 120-126, <https://doi.org/10.1016/j.jsg.2018.01.007>, 2018.



Table 1 Summary of experiments

Sample No.	Temperature	Initial length	True axial strain	Peak stress (corrected)	Strain rate at peak stress	True axial strain at peak stress	Final stress (corrected)	Final strain rate
	T (°C)	L_0 (mm)	(ϵ)	σ_p (MPa)	$\dot{\epsilon}_p$ (s ⁻¹)	ϵ_p	σ_f (MPa)	$\dot{\epsilon}_f$ (s ⁻¹)
PIL176	-10	30.480	0.03	1.78	1.03×10^{-5}	0.02	1.70	1.04×10^{-5}
PIL163	-10	48.768	0.05	2.92	1.03×10^{-5}	0.01	2.42	1.06×10^{-5}
PIL178	-10	39.624	0.08	2.54	1.11×10^{-5}	0.02	1.97	1.19×10^{-5}
PIL177	-10	40.640	0.12	2.85	1.11×10^{-5}	0.03	1.90	1.21×10^{-5}
¹ PIL007	-10	63.754	0.19	2.13	1.03×10^{-5}	0.02	1.33	1.22×10^{-5}
PIL254	-20	39.624	0.03	4.33	1.05×10^{-5}	0.02	4.25	1.06×10^{-5}
PIL182	-20	46.990	0.04	4.88	8.09×10^{-6}	0.02	4.44	8.94×10^{-6}
PIL184	-20	31.242	0.08	3.64	1.13×10^{-5}	0.04	3.24	1.17×10^{-5}
PIL185	-20	41.656	0.12	4.69	1.09×10^{-5}	0.03	3.68	1.19×10^{-5}
PIL255	-20	49.530	0.20	4.66	1.10×10^{-5}	0.03	2.93	1.28×10^{-5}
PIL165	-30	37.846	0.03	8.24	1.08×10^{-5}	0.03	8.15	1.09×10^{-5}
PIL162	-30	50.546	0.05	8.71	1.07×10^{-5}	0.03	7.87	1.10×10^{-5}
PIL164	-30	45.974	0.07	8.93	1.03×10^{-5}	0.03	7.31	1.07×10^{-5}
PIL166	-30	45.466	0.12	7.60	1.11×10^{-5}	0.03	6.45	1.20×10^{-5}
PIL268	-30	47.240	0.21	7.82	1.10×10^{-5}	0.02	5.00	1.31×10^{-5}

¹ Experiment from study by Qi and others (2017).



Table 2 Summary of EBSD analyses

Sample No.	T (°C)	Data with 30 μm step size				Data with 5 μm step size			
		Map area (Width \times Length (mm))	No. indexed	No. grains	M-index for all indexed pixels	Map area (Width \times Length (mm))	No. indexed	No. grains	M-index for all indexed pixels
PIL176	-10	25.00 \times 25.00	353781	4728	0.00119	5.41 \times 4.00	785025	694	0.010244
PIL163	-10	24.53 \times 10.28	201134	4851	0.00858	6.80 \times 4.16	992513	1494	0.008886
PIL178	-10	16.20 \times 20.30	235789	6270	0.05765	5.50 \times 4.11	690117	1028	0.046907
PIL177	-10	16.67 \times 15.38	163507	5018	0.04068	5.49 \times 4.14	645076	1507	0.040403
¹ PIL007	-10	13.10 \times 5.87	91830	1655	0.12457	1.88 \times 12.43	1010898	1789	0.118133
PIL254	-20	34.26 \times 9.33	166929	2735	0.00227	5.41 \times 4.24	641292	903	0.006909
PIL182	-20	36.58 \times 6.04	213919	4053	0.00540	5.48 \times 4.28	691817	907	0.004948
PIL184	-20	21.09 \times 7.14	120209	2440	0.01296	5.50 \times 4.13	665454	1157	0.010872
PIL185	-20	26.36 \times 7.92	121589	3127	0.01541	5.56 \times 4.23	625128	3023	0.019941
PIL255	-20	12.42 \times 7.95	25644	1213	0.101764	3.41 \times 4.20	472774	3057	0.106619
PIL165	-30	19.57 \times 14.78	258779	4728	0.00077	5.45 \times 3.07	594671	589	0.006147
PIL162	-30	25.96 \times 10.00	191672	4833	0.00442	8.11 \times 3.97	937793	2399	0.004555
PIL164	-30	18.22 \times 22.56	229261	6087	0.02164	4.04 \times 5.55	598744	1515	0.017329
PIL166	-30	31.26 \times 18.29	415185	8878	0.02334	8.08 \times 3.98	1043672	6036	0.020205
PIL268	-30	5.76 \times 20.76	93394	1039	0.101730	5.69 \times 10.18	1664877	8215	0.063540

¹ Experiment from study by Qi and others (2017).



Table 3 Summary of subgrain and grain sizes

Sample No.	T (°C)	${}^2\varepsilon$	${}^3\bar{d}$ (μm)				${}^5\bar{D}$ (μm)	${}^6D_{SMR}$ (μm)	${}^7\overline{D}_{big}$ (μm)	${}^8\overline{D}_{small}$ (μm)	${}^9D_{peak}$ (μm)	${}^{10}d_{Speak}$ (μm)	${}^{11}\zeta_{diff}$
			${}^4\varphi \geq 2^\circ$	$\varphi \geq 4^\circ$	$\varphi \geq 6^\circ$	$\varphi \geq 8^\circ$							
PIL176	-10	0.03	134	146	132	155	156	132	250	51	30	20	0.4
PIL163	-10	0.05	104	118	110	124	125	110	197	58	35	25	0.6
PIL178	-10	0.08	127	135	127	140	140	127	194	63	55	50	0.5
PIL177	-10	0.12	96	106	101	113	114	101	184	59	40	30	0.6
¹ PIL007	-10	0.19	96	101	96	105	106	96	174	58	50	45	0.6
PIL254	-20	0.03	91	102	93	112	114	93	197	38	25	20	0.4
PIL182	-20	0.04	103	129	131	146	148	131	188	42	30	25	0.4
PIL184	-20	0.08	88	105	105	119	122	105	169	42	45	20	0.5
PIL185	-20	0.12	55	63	66	71	75	66	132	41	30	20	0.8
PIL255	-20	0.20	55	59	59	63	64	59	106	41	30	25	0.8
PIL165	-30	0.03	108	126	126	145	149	126	203	38	40	20	0.4
PIL162	-30	0.05	70	84	91	99	103	91	144	40	35	20	0.6
PIL164	-30	0.07	59	72	82	91	98	82	158	39	30	20	0.7
PIL166	-30	0.12	57	60	61	65	67	61	104	70	35	25	1.2
PIL268	-30	0.21	42	46	50	55	60	50	158	35	30	20	0.8

¹ Experiment from study by Qi and others (2017). ² True axial strain. ³ Mean subgrain size. ⁴ Boundary misorientation angle. ⁵ Mean grain size. ⁶ Square mean root grain size. ⁷ Mean grain size of “big grains”. ⁸ Mean grain size of “small grains”. ⁹ Peak grain size in grain size distribution. ¹⁰ Peak grain size in subgrain size (with $\varphi \geq 2^\circ$) distribution. ¹¹ Ratio between \overline{D}_{small} and \bar{d} at $\varphi \geq 2^\circ$.



Table 4 Summary of the open half-angle of the *c*-axis cone (θ) from this study and the literature

Reference	Name	Material	T (°C)	No. of <i>c</i> -axes	θ (°)	Conditions*	True axial strain rate converted (s^{-1}) – at the end of experiment	True axial strain converted (%) – at the end of experiment	
This study	PIL163	H ₂ O	-10	353781	40	$\varepsilon = 5\%$	1.06×10^{-5}	5.0	
	PIL178	H ₂ O	-10	201134	36	$\varepsilon = 8\%$	1.19×10^{-5}	8.0	
	PIL177	H ₂ O	-10	235789	36	$\varepsilon = 12\%$	1.21×10^{-5}	12.0	
	PIL007	H ₂ O	-10	163507	34	$\varepsilon = 19\%$	1.22×10^{-5}	19.0	
	PIL182	H ₂ O	-20	213919	30	Constant displacement rate $\dot{\varepsilon} = \sim 1 \times 10^{-5} s^{-1}$	$\varepsilon = 4\%$	8.94×10^{-6}	4.0
	PIL184	H ₂ O	-20	120209	26		$\varepsilon = 8\%$	1.17×10^{-5}	8.0
	PIL185	H ₂ O	-20	121589	28		$\varepsilon = 12\%$	1.19×10^{-5}	12.0
	PIL255	H ₂ O	-20	25644	32		$\varepsilon = 20\%$	1.28×10^{-5}	20.0
	PIL164	H ₂ O	-30	229261	14		$\varepsilon = 7\%$	1.07×10^{-5}	7.0
	PIL166	H ₂ O	-30	415185	16		$\varepsilon = 12\%$	1.20×10^{-5}	12.0
PIL268	H ₂ O	-30	93394	8		$\varepsilon = 21\%$	1.31×10^{-5}	21.0	
Jacka and Maccagnan (1984)	A2	H ₂ O	-3	132	42	Constant load $\sigma = \sim 0.2$ MPa	$\dot{\gamma} = 3.6 \times 10^{-8} s^{-1}, \gamma = 2.4\%$	5.17×10^{-8}	3.4
	A3	H ₂ O	-3	98	36		$\dot{\gamma} = 4.0 \times 10^{-8} s^{-1}, \gamma = 2.9\%$	5.77×10^{-8}	4.1
	A4	H ₂ O	-3	111	28		$\dot{\gamma} = 6.1 \times 10^{-8} s^{-1}, \gamma = 6.8\%$	9.04×10^{-8}	9.8
	A5	H ₂ O	-3	95	36		$\dot{\gamma} = 6.3 \times 10^{-8} s^{-1}, \gamma = 7.3\%$	9.37×10^{-8}	10.6
	A6	H ₂ O	-3	108	26		$\dot{\gamma} = 6.1 \times 10^{-8} s^{-1}, \gamma = 15.0\%$	9.53×10^{-8}	22.3
	A7	H ₂ O	-3	96	30		$\dot{\gamma} = 6.0 \times 10^{-8} s^{-1}, \gamma = 32.5\%$	1.02×10^{-7}	51.0
Jacka and Li (2000)	N/A	H ₂ O	-5	87	26	Constant load, $\sigma = 0.2$ MPa	$\dot{\gamma} = 3.4 \times 10^{-8} s^{-1}, \gamma = 11.0\%$	5.18×10^{-8}	16.2
	N/A	H ₂ O	-10	100	32	Constant load, $\sigma = 0.2$ MPa	$\dot{\gamma} = 6.6 \times 10^{-9} s^{-1}, \gamma = 10.0\%$	9.99×10^{-9}	14.6
	N/A	H ₂ O	-15	173	38	Constant load, $\sigma = 0.5$ MPa	$\dot{\gamma} = 7.5 \times 10^{-8} s^{-1}, \gamma = 11.0\%$	1.14×10^{-7}	16.2
	N/A	H ₂ O	-15	199	32	Constant load, $\sigma = 0.4$ MPa	$\dot{\gamma} = 3.6 \times 10^{-8} s^{-1}, \gamma = 11.0\%$	5.49×10^{-8}	16.2
Piazolo et al (2013)	MD6	D ₂ O	-7	N/A	35	Constant displacement rate	$\dot{e} = 6 \times 10^{-7} s^{-1}, e = 10\%$	6.67×10^{-7}	11.0
	MD10	D ₂ O	-7	N/A	35		$\dot{e} = 2.5 \times 10^{-6} s^{-1}, e = 10\%$	2.78×10^{-6}	11.0
	MD3	D ₂ O	-7	N/A	35		$\dot{e} = 2.5 \times 10^{-6} s^{-1}, e = 20\%$	3.13×10^{-6}	22.0
	MD12	D ₂ O	-7	N/A	35		$\dot{e} = 1.0 \times 10^{-5} s^{-1}, e = 10\%$	1.11×10^{-5}	11.0
	MD4	D ₂ O	-7	N/A	35		$\dot{e} = 1.0 \times 10^{-5} s^{-1}, e = 20\%$	1.25×10^{-5}	22.0
	MD22	D ₂ O	-7	N/A	30		$\dot{e} = 1.0 \times 10^{-5} s^{-1}, e = 40\%$	1.67×10^{-5}	51.0
Montagnat et al (2015)	N/A	H ₂ O	-5	2838	40	Constant load, $\sigma = 0.8$ MPa	$\dot{e} = 1.2 \times 10^{-7} s^{-1}, e = 7\%$	1.30×10^{-7}	7.0
	N/A	H ₂ O	-5	N/A	35	Constant load, $\sigma = 0.75$ MPa	$\dot{e} = 3.9 \times 10^{-7} s^{-1}, e = 12\%$	4.43×10^{-7}	12.8
	N/A	H ₂ O	-5	1862	35	Constant load, $\sigma = 0.7$ MPa	$\dot{e} = 3.8 \times 10^{-7} s^{-1}, e = 13\%$	4.37×10^{-7}	13.9
	N/A	H ₂ O	-5	830	33	Constant load, $\sigma = 0.8$ MPa	$\dot{e} = 3.8 \times 10^{-7} s^{-1}, e = 18\%$	4.63×10^{-7}	19.9



Qi et al (2017)	PIL7	H ₂ O	-10	N/A	37	Constant displacement rate	$\dot{\epsilon} = \sim 1 \times 10^{-5} s^{-1}, \epsilon = 18\%$	1.10×10^{-5}	18.0	
	PIL32	H ₂ O	-10	N/A	34		$\dot{\epsilon} = \sim 2 \times 10^{-6} s^{-1}, \epsilon = 21\%$	2.31×10^{-6}	21.0	
	PIL33	H ₂ O	-10	N/A	26		$\dot{\epsilon} = \sim 2 \times 10^{-4} s^{-1}, \epsilon = 22\%$	2.42×10^{-4}	22.0	
	PIL35	H ₂ O	-10	N/A	35		$\dot{\epsilon} = \sim 1 \times 10^{-5} s^{-1}, \epsilon = 13\%$	1.35×10^{-5}	13.0	
	PIL36	H ₂ O	-10	N/A	34		$\dot{\epsilon} = \sim 5 \times 10^{-5} s^{-1}, \epsilon = 19\%$	5.02×10^{-5}	19.0	
Vaughan et al (2017)	def013	H ₂ O	-5	206641	42	Constant displacement rate	$e = 3\%$	1.03×10^{-6}	3.0	
	def012	H ₂ O	-5	309428	36		$e = 5\%$	1.05×10^{-6}	5.1	
	def011	H ₂ O	-5	218653	38		$\dot{\epsilon} = \sim 1 \times 10^{-6} s^{-1}$	$e = 7.5\%$	1.08×10^{-6}	7.8
	def010	H ₂ O	-5	335722	34		$e = 10\%$	1.11×10^{-6}	10.5	
Craw et al (2018)	PIL133	H ₂ O	-30	N/A	0	Constant displacement rate	$\dot{\epsilon} = \sim 2 \times 10^{-6} s^{-1}, \epsilon = 20\%$	2.60×10^{-6}	20	
	PIL141	H ₂ O	-30	N/A	0		$\dot{\epsilon} = \sim 5 \times 10^{-6} s^{-1}, \epsilon = 23\%$	7.20×10^{-6}	23	
	PIL132	H ₂ O	-30	N/A	0		$\dot{\epsilon} = \sim 2 \times 10^{-5} s^{-1}, \epsilon = 20\%$	2.80×10^{-5}	20	

* $\dot{\epsilon}$ is the true axial strain rate, ϵ is the true axial strain, $\dot{\gamma}$ is the octahedral shear strain rate, γ is the octahedral shear strain, \dot{e} is the engineering axial strain rate, e is the engineering axial strain, σ is the initial stress.

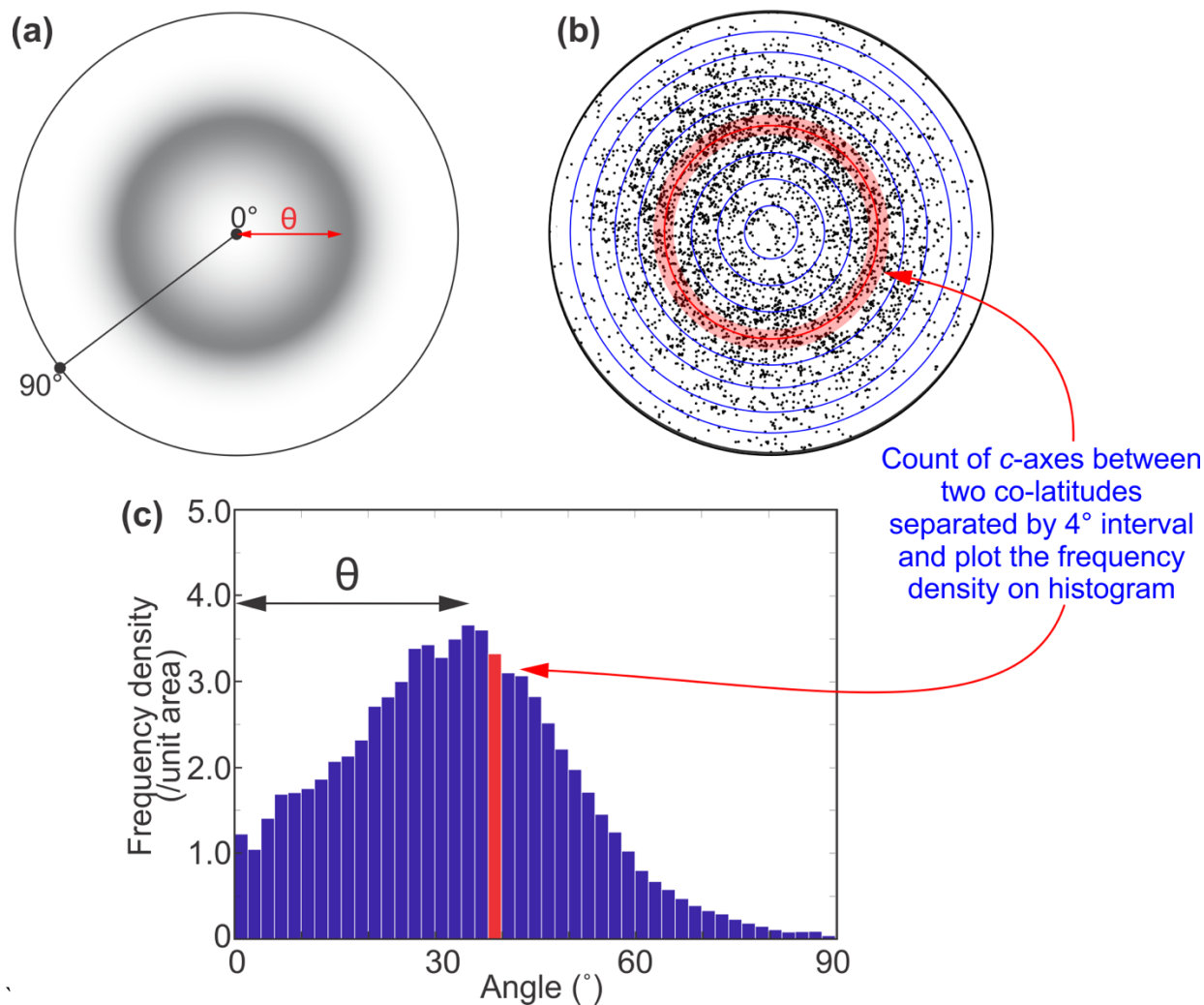


Figure 1. (a) Typical *c*-axes distribution at high temperatures with compression axis perpendicular to the page. (b) A schematic drawing explaining the method used to quantify the distribution of *c*-axes. The *c*-axes point pole figure taken from PIL178 is used as an example. The pole figure is plotted with lower hemisphere equal-area projection, and compression axis perpendicular to the page. Only 3000 points are plotted for demonstration purpose. At a given angle, red circles between co-latitudes separated by 4 degrees' interval were drawn. The points lying between the given co-latitudes (red area) are counted. The frequency density of the points is calculated from the normalised counts divided by the normalised area between the given co-latitudes. (c) The distribution of *c*-axes frequency density as a function of angle to the compression axis. The angle corresponds to the peak in the distribution is taken as the opening half-angle θ for the cone (small circle) shaped *c*-axes distribution. Throughout the text this is referred to as the opening-angle.



5

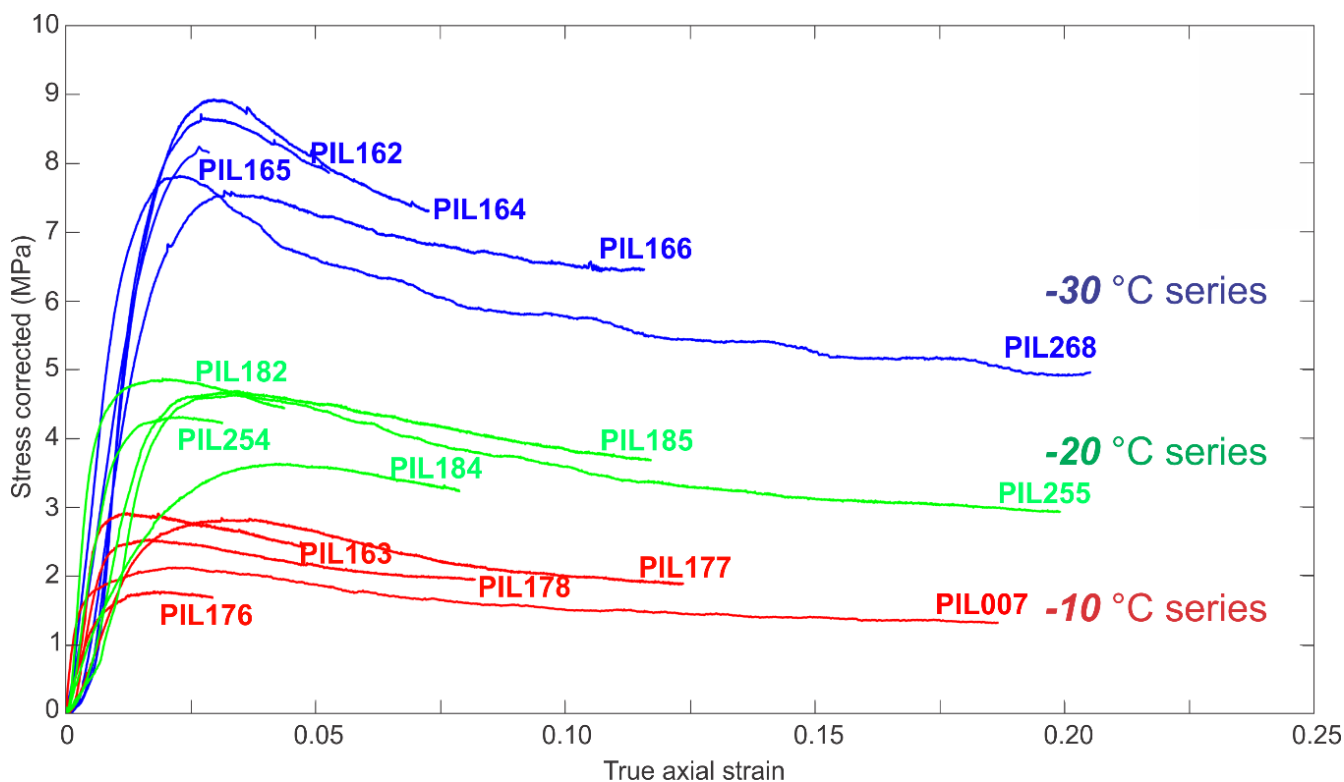


Figure 2. The stress-strain curves for all the deformed ice samples. The x -axis is the true axial strain (Eq. (2)). The y -axis is the uniaxial stress. The stress has been corrected for the change of sample cross-sectional area, assuming constant sample volume during the deformation.

10

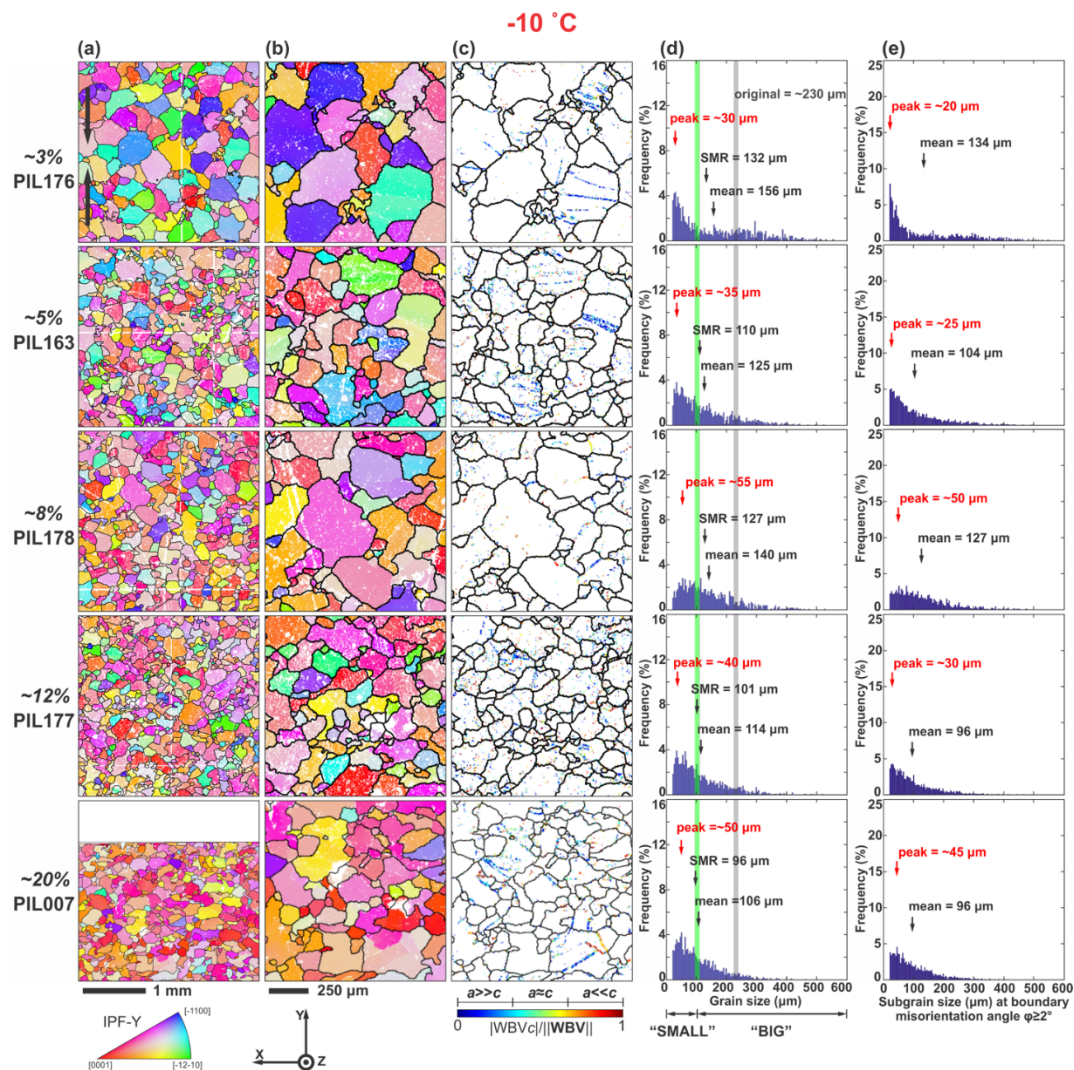


Figure 3. Microstructural analyses of deformed ice samples at $-10\text{ }^{\circ}\text{C}$. Axial true strain increases from $\sim 3\%$ on top to $\sim 20\%$ to bottom. The EBSD data collected with $5\text{ }\mu\text{m}$ step size are presented as (a) orientation maps at low magnification and (b) orientation maps of selected areas at high magnification. Orientation maps are coloured by IPF-Y, which uses the colour map to indicate the crystallographic axes that are parallel to the vertical shortening direction as shown by the black arrows. Ice grain boundaries with a misorientation larger than 10° are shown black. Non-indexed pixels are shown white. Maps show data without interpolation. (c) Distribution of sub-grain boundaries with each pixel coloured by the ratio of c -component WBV (ϕ_{WBVc}), which increases from 0 (blue) to 1 (red). Grain boundaries are shown in black. (d) Distribution of ice grain size presented in $4\text{ }\mu\text{m}$ bins. Mean and square mean root (SMR) diameters are indicated by black arrows. The main peak of the grain size distribution is indicated by a red arrow. Vertical grey line marks the mean grain size of the starting material. Vertical

green line marks the threshold grain size between “big grains” and “small grains” (see text). (e) Distribution of subgrain size presented in 4 μm bins. The subgrain size is calculated by applying the boundary misorientation angle of $\varphi \geq 2^\circ$.

5

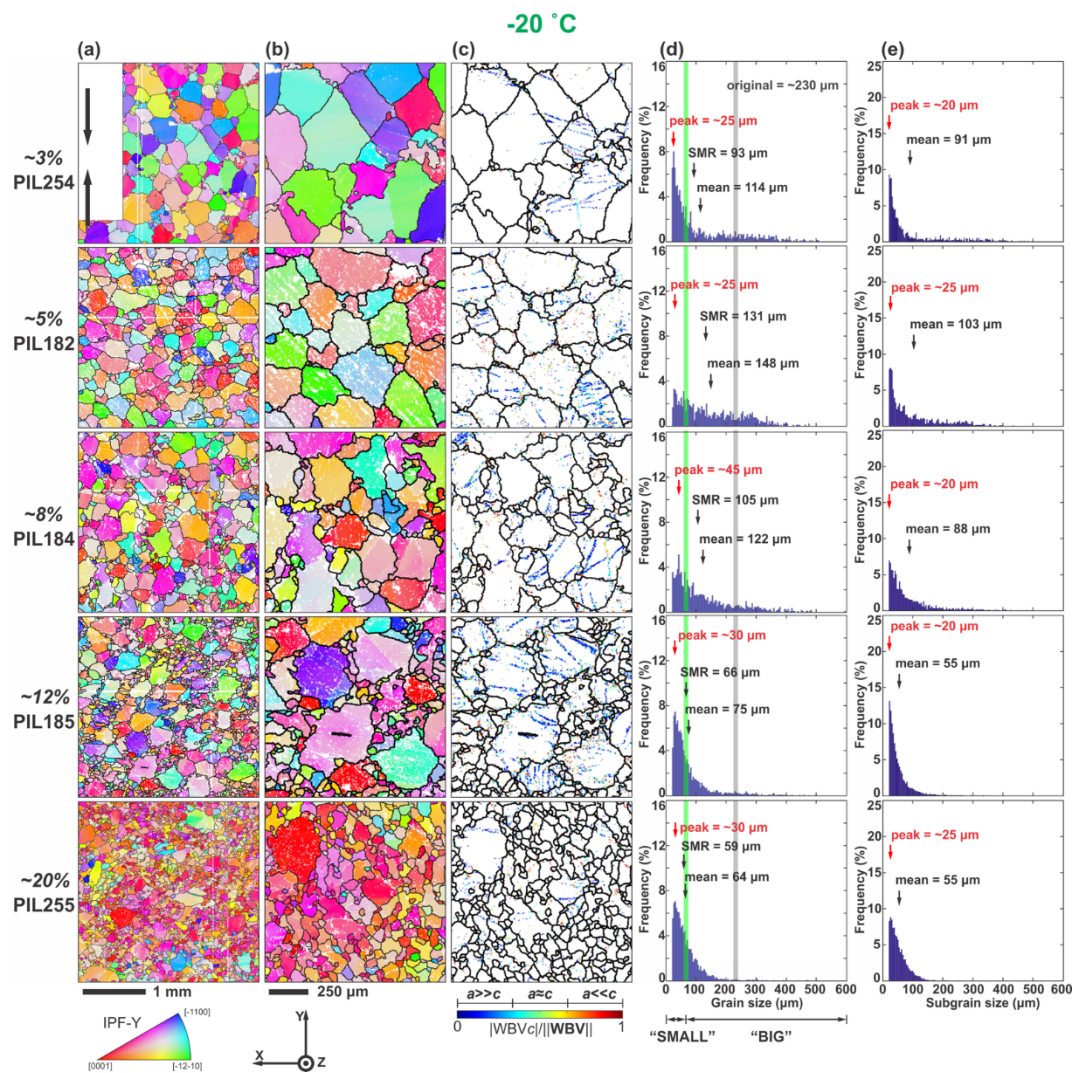
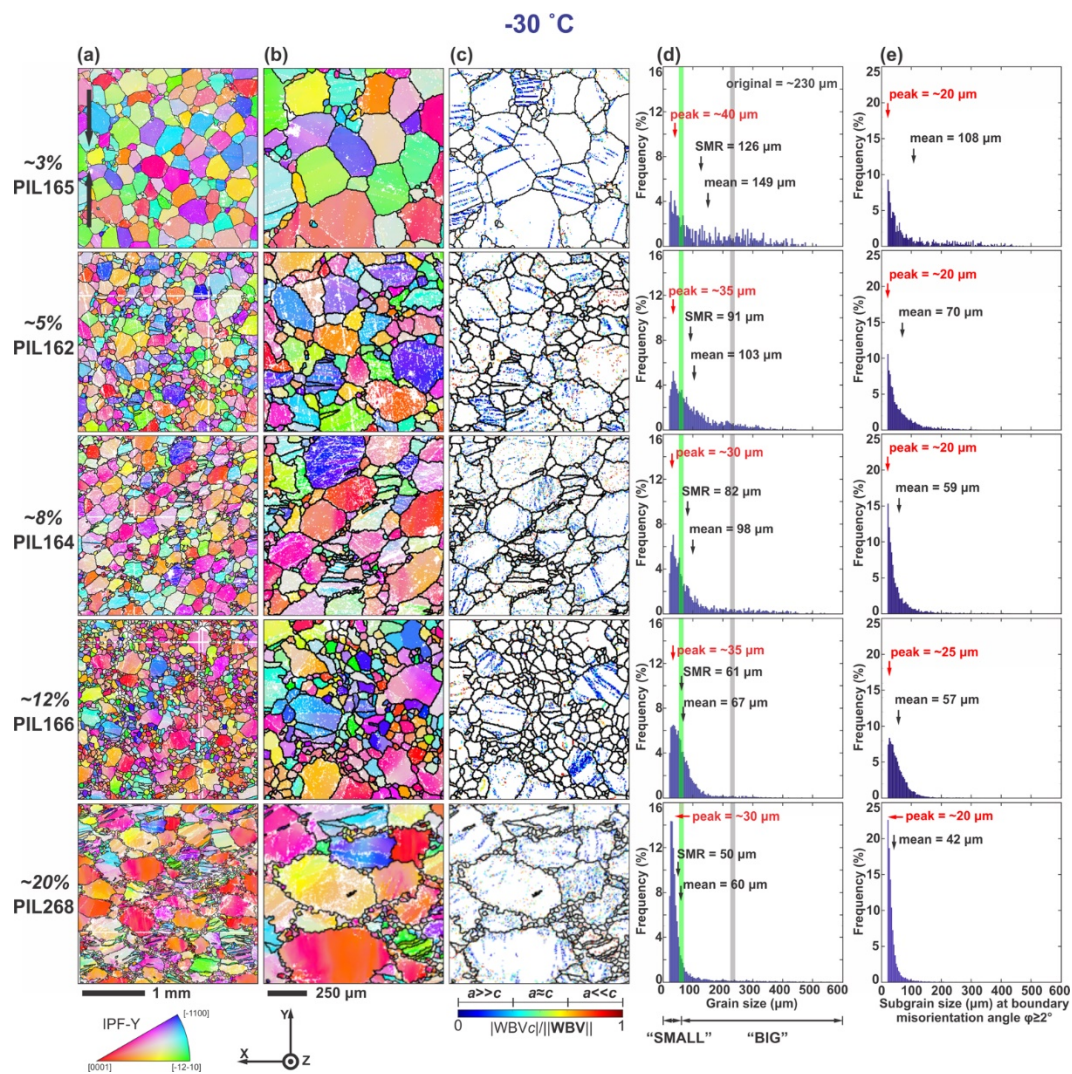


Figure 4. Microstructural analyses of deformed ice samples at -20°C . Axial true strain increases from $\sim 3\%$ on top to $\sim 20\%$ to bottom. The descriptions of columns (a) to (e) are the same as in Fig. 3.

10



5 **Figure 5.** Microstructural analyses of deformed ice samples at -30 °C. Axial true strain increases from ~3% on top to ~20% to bottom. The descriptions of columns (a) to (e) are the same as in Fig. 3.

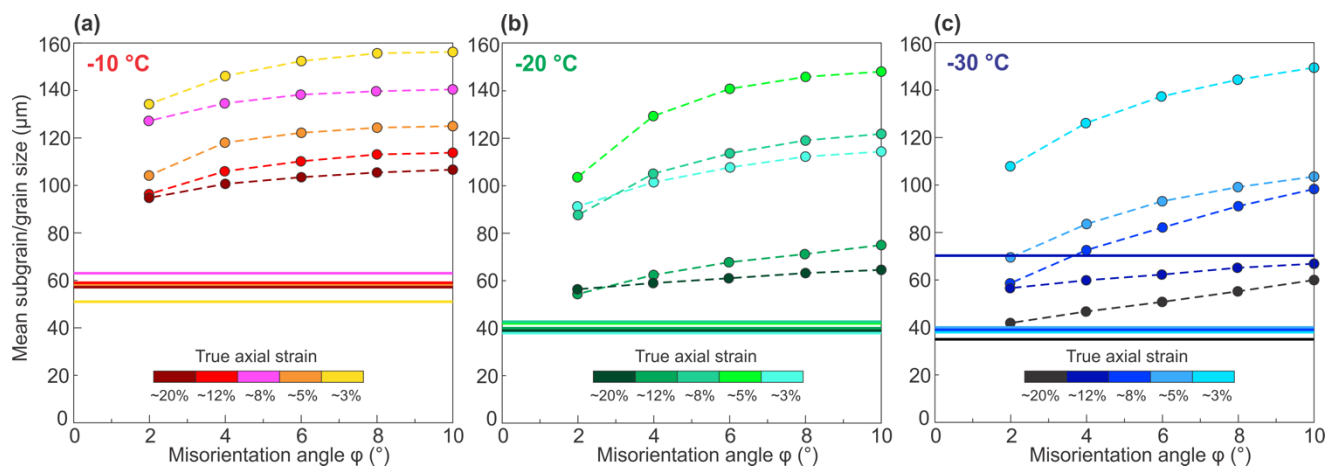


Figure 6. Mean subgrain/grain size (circles) as a function of boundary misorientation angle φ . Mean subgrain sizes are calculated with $\varphi \geq 2^\circ$, 4° , 6° and 8° . Mean grain size is calculated with $\varphi \geq 10^\circ$. Mean grain sizes for “small grains” are marked with horizontal solid lines.

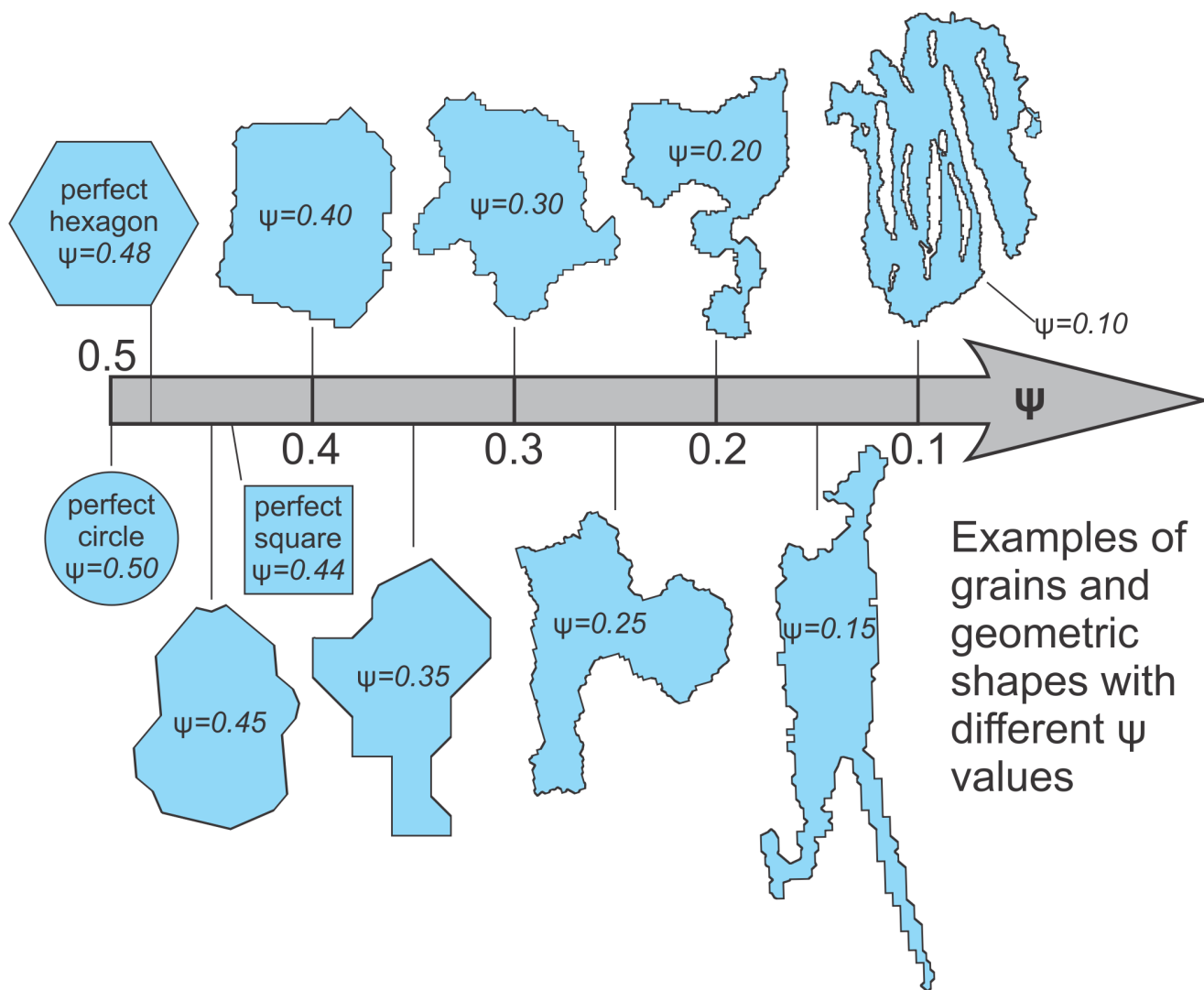


Figure 7. Illustration of grains and geometric shapes with different sphericity parameter Ψ values. The Ψ is introduced to quantify the ice grain boundary lobateness (see text).

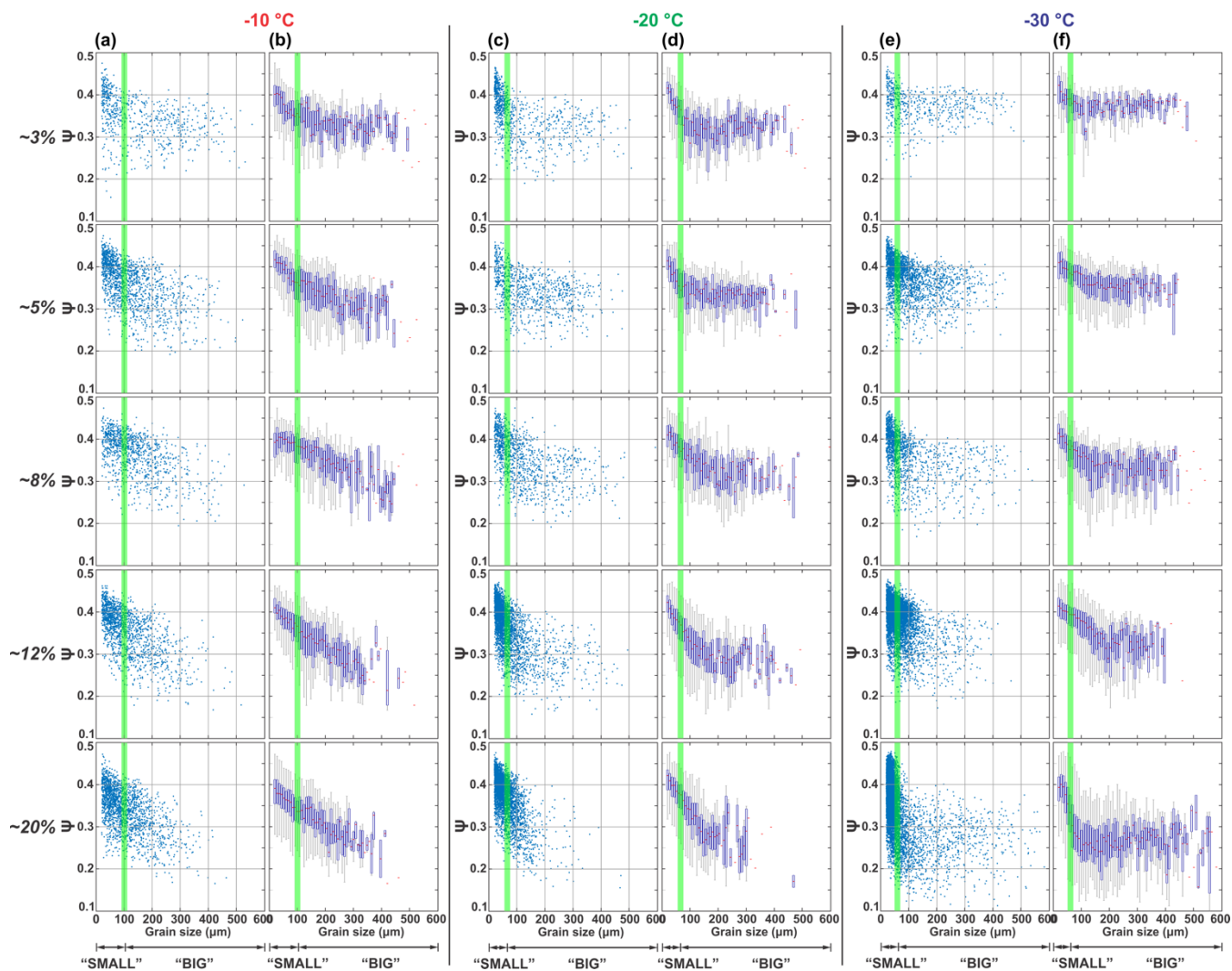


Figure 8. The relationship between grain boundary sphericity parameter Ψ and grain size. Scattered plots of Ψ as a function of grain size are shown in (a), (c) and (e). The interquartile ranges (IQRs) of the Ψ values within grain size bins of 4 μm are shown in (b), (d) and (f). The IQR is visualised as box plot, the box covers the interquartile range and represents 50% of the total data, the red line within the box is the median point and the whiskers are the extremes (3/2s of the interquartile range). Vertical green lines mark the threshold grain size between “big grains” and “small grains” (see text).

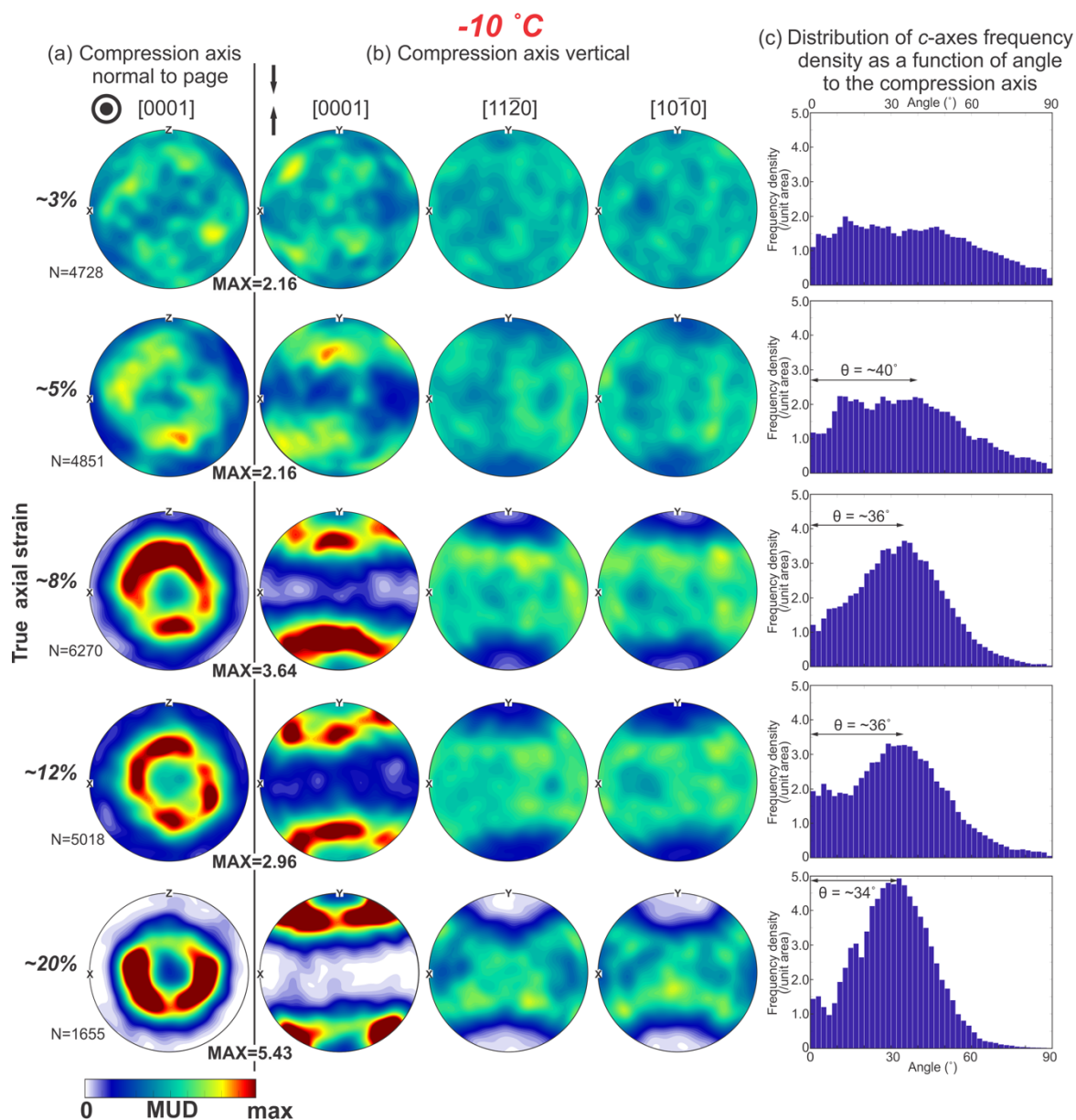


Figure 9. Crystallographic preferred orientations (CPOs) from EBSD data with 30 μm step size for ice samples deformed at $-10\text{ }^{\circ}\text{C}$. Axial true strain increases from $\sim 3\%$ on top to $\sim 20\%$ to bottom. The number of grains is marked on the bottom left for each sample. **(a)** The distributions of $[0001]$ (c -axes) orientations, with the compression axis perpendicular to the page. **(b)** The distributions of orientations for $[0001]$ (c -axes), $[11\bar{2}0]$ a -axes and $[10\bar{1}0]$ (m -axes), with the compression axis vertical. The maximum value of MUD for the c -axis CPO of each sample is given between columns (a) and (b). **(c)** Distributions of the $[0001]$ axes frequency density as a function of angle to the compression axis. Open half-angle θ of the cone (small circle) is presented on each histogram.

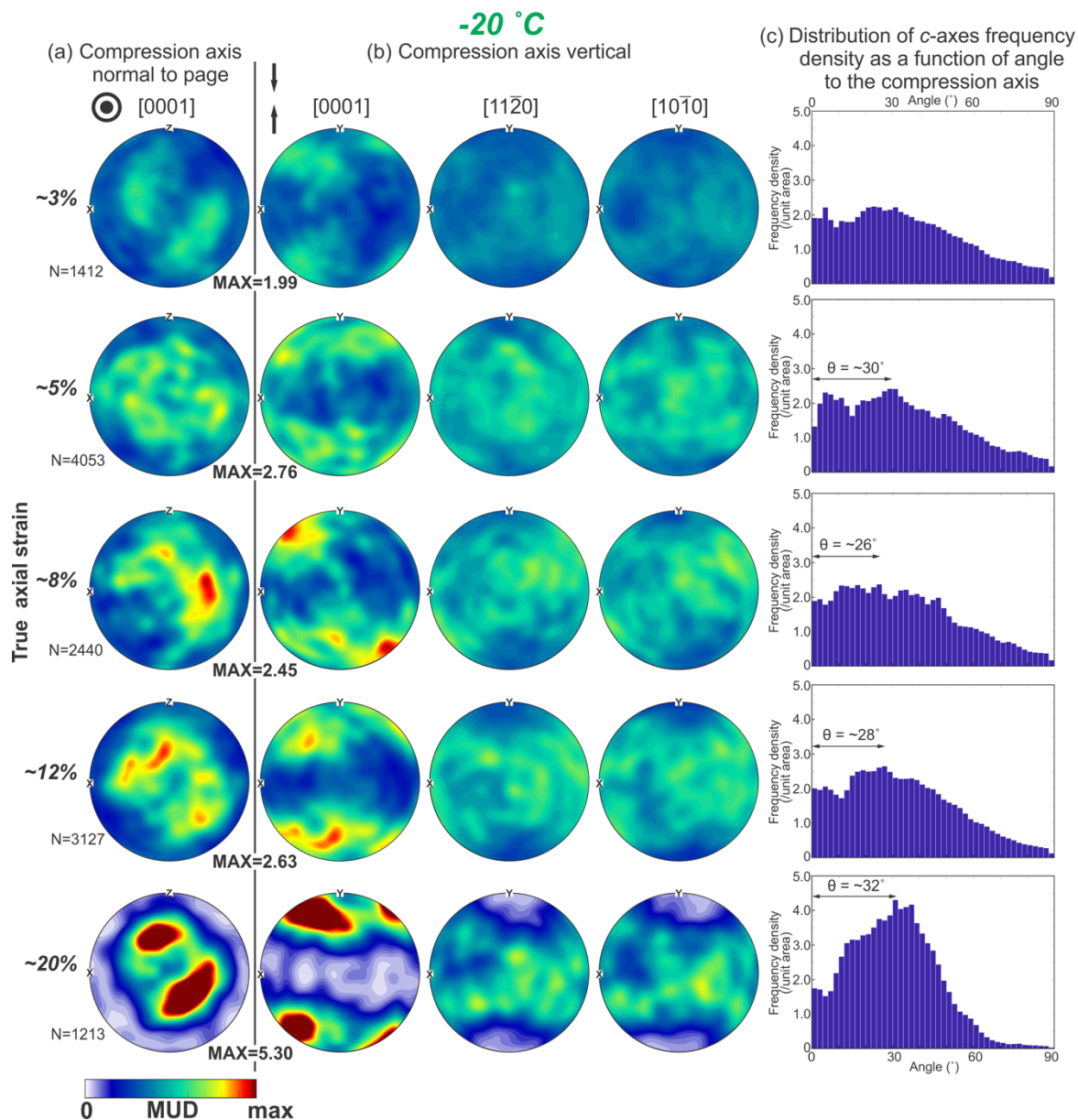


Figure 10. Crystallographic preferred orientations (CPOs) from EBSD data with 30 μm step size for ice samples deformed at $-20\text{ }^{\circ}\text{C}$. Explanation of annotations and the descriptions of sections (a) to (c) are the same as in Fig. 9.

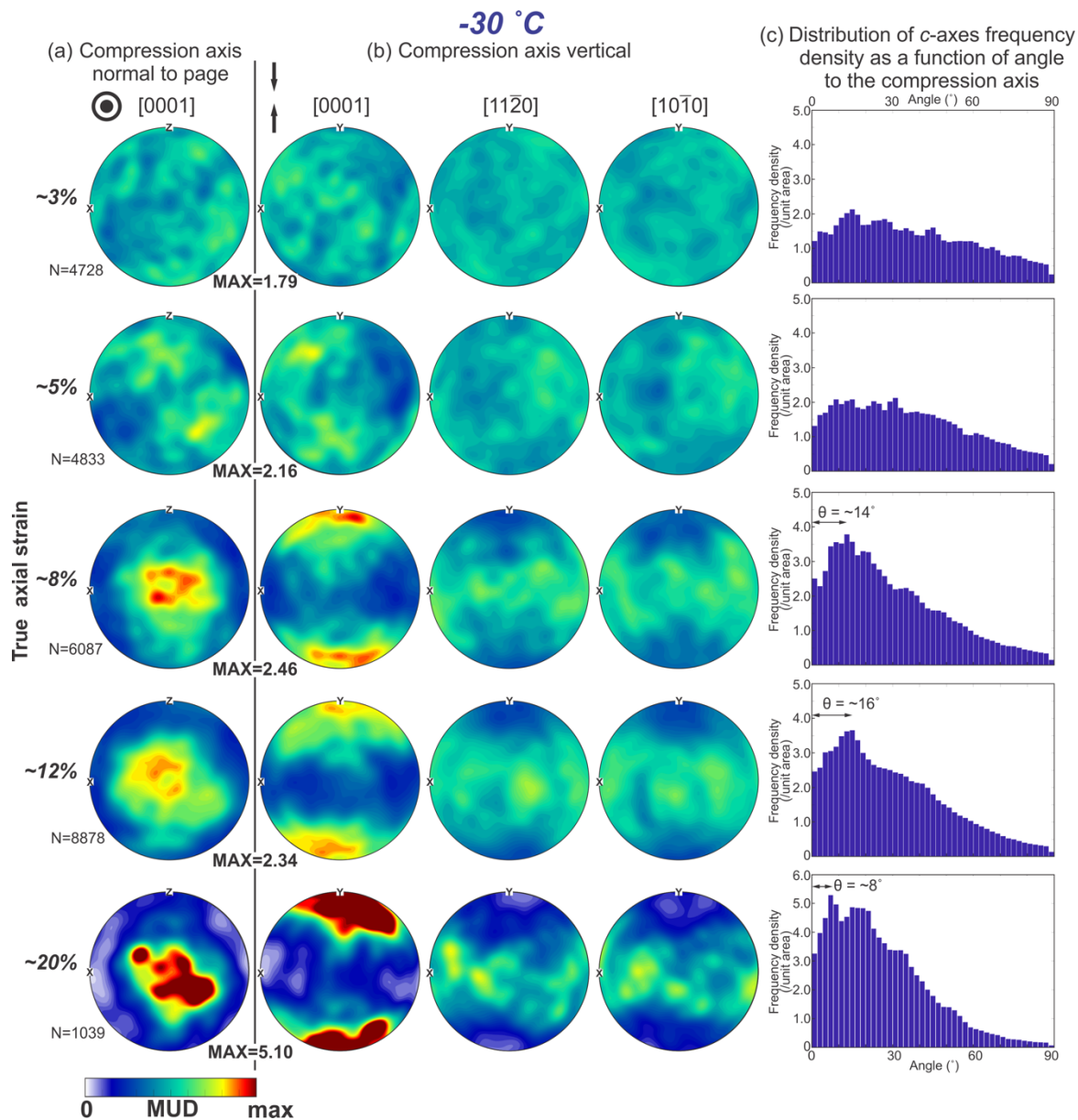


Figure 11. Crystallographic preferred orientations (CPOs) from EBSD data with 30 μm step size for ice samples deformed at $-30\text{ }^{\circ}\text{C}$. Explanation of annotations and the descriptions of sections (a) to (c) are the same as in Fig. 9.

5

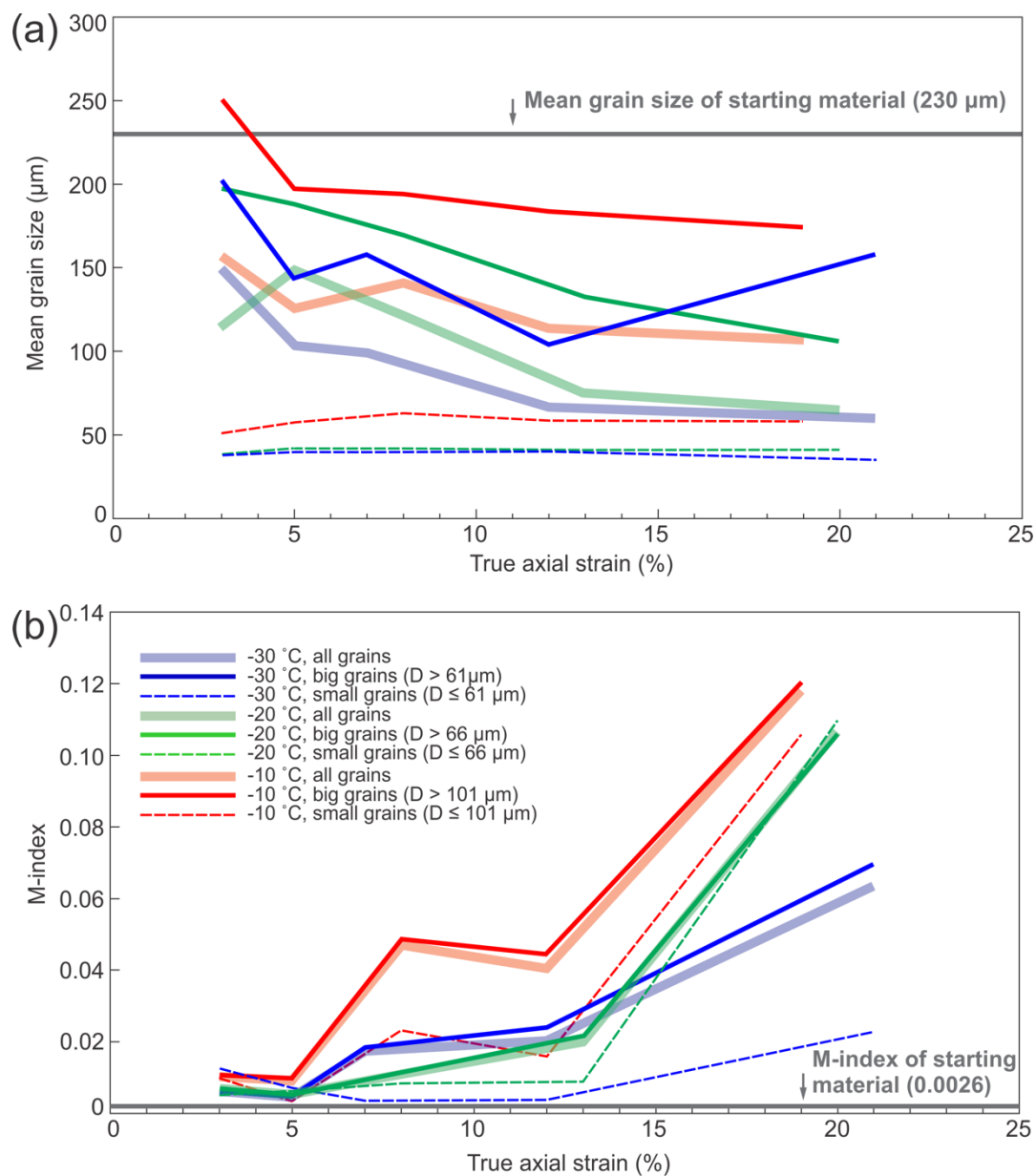
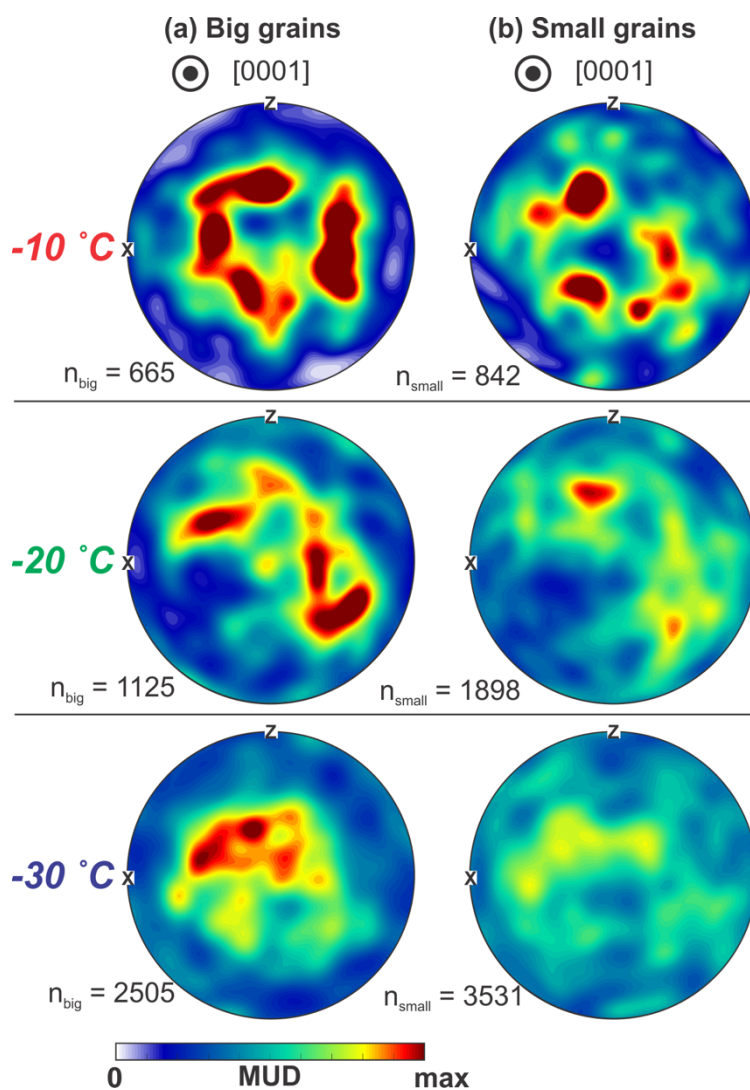
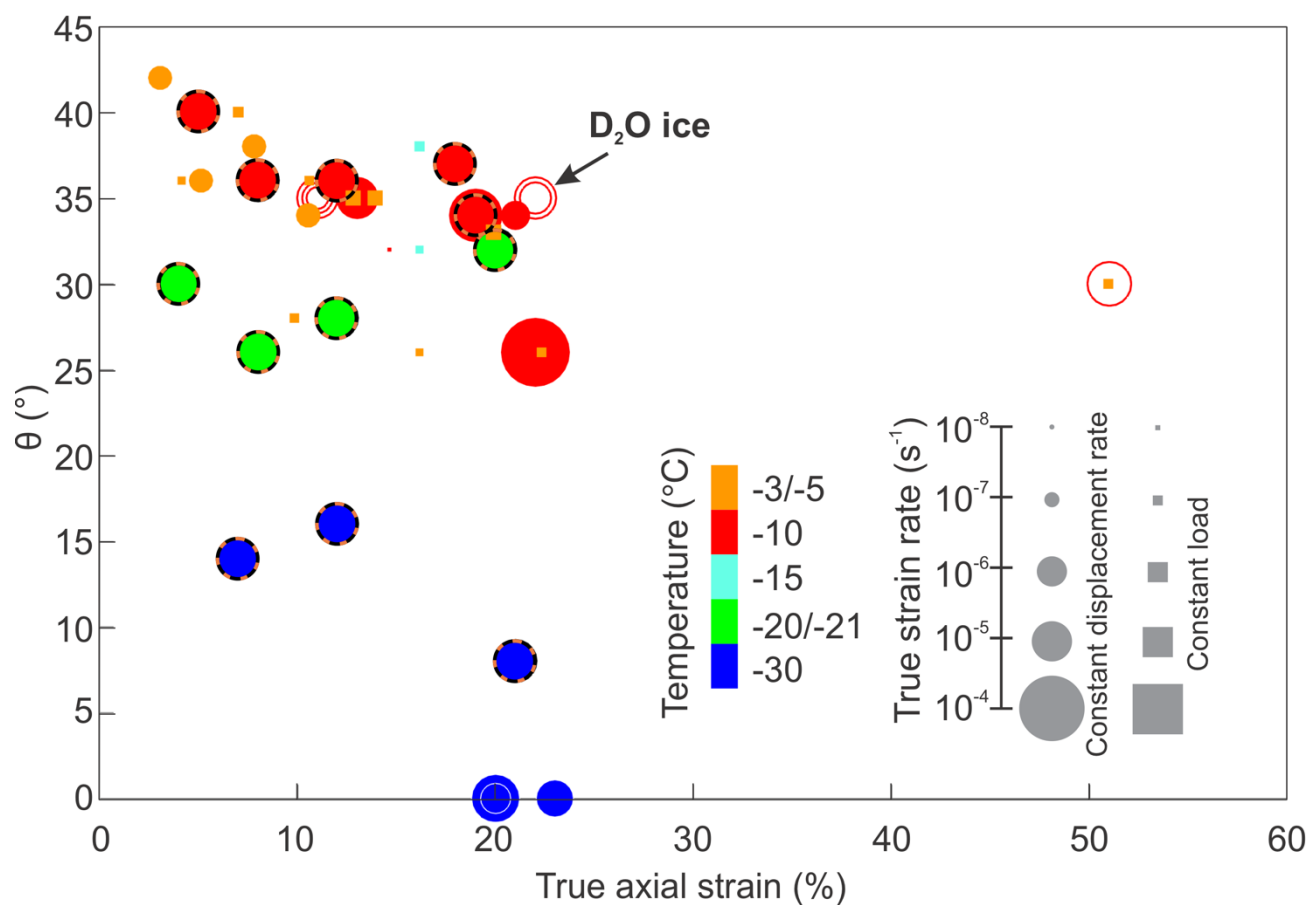


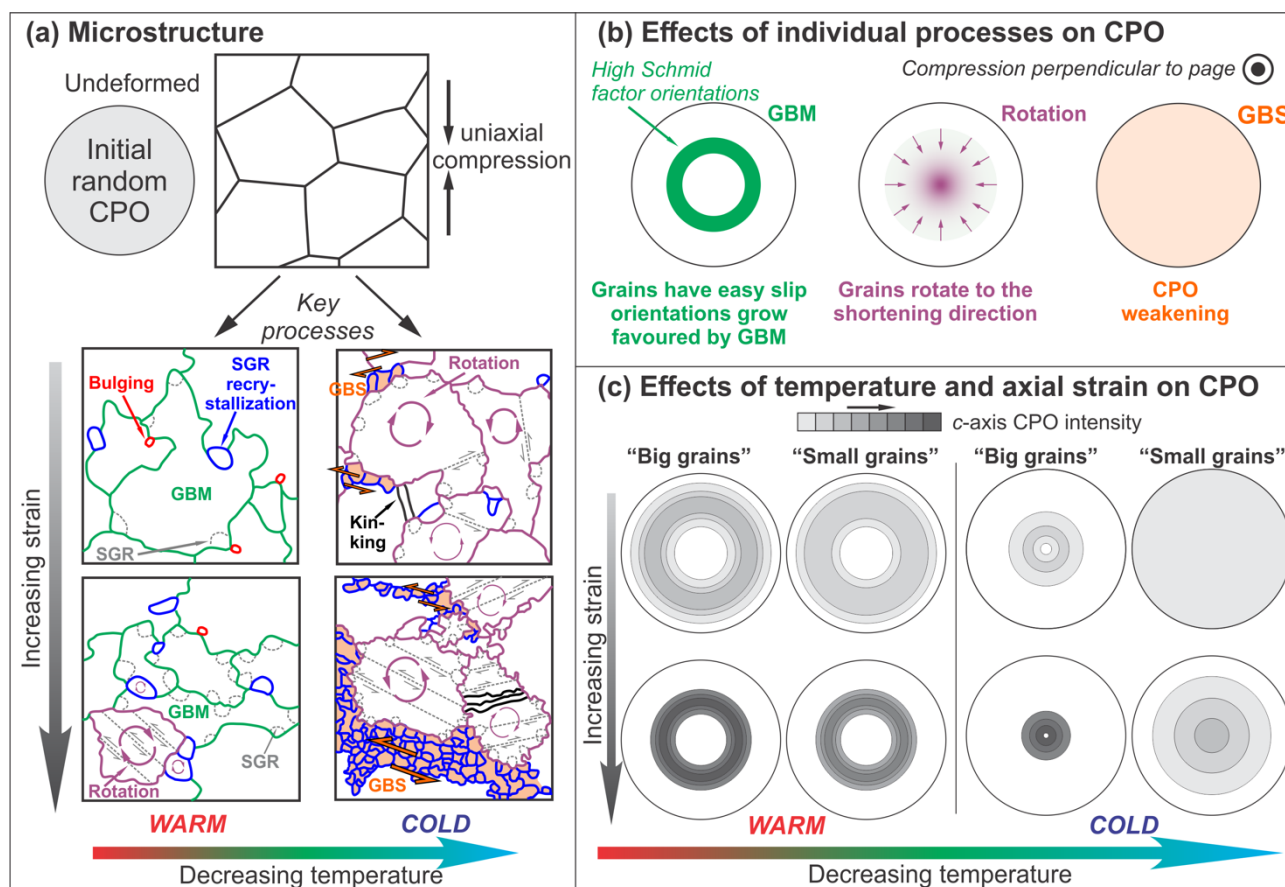
Figure 12. (a) Variation in the mean grain size as a function of true axial strain for different grain size categories in each temperature series. (b) Variation in CPO strength (M-index) as a function of true axial strain for different grain size categories in each temperature series.



5 **Figure 13.** Comparison of contoured [0001] (*c*-axis) CPOs of (a) “big grains” and (b) “small grains”, for the samples deformed to ~12% strain at different temperatures. The numbers of “big grains” and “small grains” are marked on the bottom left of pole figures. The *c*-axis CPOs are calculated based on all pixels taken from the EBSD data with 5 μm step size. Compression axis is in the centre of the stereonets.



5 **Figure 14.** Plot of the relationship between the opening-angle, θ , of the cone-shaped *c*-axis CPO and the true strain. The data
come from this study and the literature (Table 4). The data from constant displacement rate experiments on D₂O ice (Piazolo
et al, 2013) are illustrated by hollow circles. The deformation of D₂O ice at -7 °C is a direct analogue for deforming H₂O ice
at -10 °C (Wilson et al., 2019). The data from constant displacement rate experiments on H₂O ice (this study, Vaughan et al.,
2017, Qi et al., 2017, Craw et al., 2018) are illustrated by filled circles. Data from this study are highlighted by orange-black
10 edges. The data from constant load experiments (Jacka and Maccagnan, 1984; Jacka and Li, 2000; Montagnat et al., 2015) are
illustrated by solid squares. Each marker is sized and coloured by the corresponding true strain rate and temperature,
respectively. For all experiments the strain rate shown is the strain rate at the end of the experiment.



5 **Figure 15.** Schematic drawing of the microstructure and CPO development in ice deformed under uniaxial compression. **(a)** The effects of temperature and axial strain on the microstructural evolution. Grains undergoing different deformation processes are marked by different colours, with interpretations of the processes presented. **(b)** The effects of individual processes on CPO development. **(c)** The development of CPOs for “small grains” and “big grains” with strain at different temperatures. Starting point (shown in (a)) is a random CPO. SGR: subgrain rotation. GBM: grain boundary migration. GBS: grain boundary sliding.

10